中華民國專利證書

發明第　I724578　號

發 明 名 稱：酸鹼敏感型脂質奈米粒子用於包覆抗癌藥物和微小核糖核酸及其用途

專 利 權 人：國立陽明大學

發　明　人：駱雨利

專利權期間：自2021年4月11日至2039年10月14日止

上開發明業經專利權人依專利法之規定取得專利權

經濟部智慧財產局 局長　洪淑敏

中華民國　110　年　4　月　11　日

注意：專利權人未依法繳納年費者，其專利權自原繳費期限屆滿後消滅。

IVYSPRING INTERNATIONAL PUBLISHER

Theranostics

2020; 10(15): 6695- 6714. doi: 10.7150/thno.45164

Research Paper

PEG-coated nanoparticles detachable in acidic microenvironments for the tumor-directed delivery of chemo- and gene therapies for head and neck cancer

Yu-Li Lo[1,2,3]✉, Chih-Hsien Chang[1], Chen-Shen Wang[1], Muh-Hwa Yang[4,5], Anya Maan-Yuh Lin[1,2,6], Ci-Jheng Hong[1], Wei-Hsuan Tseng[1]

1. Institute of Pharmacology, National Yang-Ming University, Taipei 11221, Taiwan.
2. Faculty of Pharmacy, National Yang-Ming University, Taipei 11221, Taiwan.
3. Center for Advanced Pharmaceutics and Drug Delivery Research, National Yang-Ming University, Taipei 11221, Taiwan.
4. Institute of Clinical Medicine, National Yang-Ming University, Taipei 11221, Taiwan.
5. Division of Medical Oncology, Department of Oncology, Taipei Veterans General Hospital, Taipei 11217, Taiwan.
6. Department of Medical Research, Taipei Veterans General Hospital, Taipei 11217, Taiwan.

✉ Corresponding author: E-mail address: yulilo@ym.edu.tw (Y.-L. Lo)

Received: 2020.02.21; Accepted: 2020.05.04; Published: 2020.05.17

Abstract

Background: Head and neck cancer (HNC) is a major cause of morbidity and mortality and has a poor treatment outcome. Irinotecan, a topoisomerase-I inhibitor, induces cell death by decreasing the religation of double-strand DNA. However, epithelial–mesenchymal transition (EMT), therapy resistance, and systemic toxicity caused by available antineoplastic agents hinder the efficacy and safety of HNC treatment. Chemotherapy combined with gene therapy shows potential application in circumventing therapy resistance and EMT. miR-200 exerts a remarkable suppressing effect on EMT-associated genes. Herein, liposomes and solid lipid nanoparticles (SLNs) modified with a pH-sensitive, self-destructive polyethylene glycol (PEG) shell and different peptides were designed as irinotecan and miR-200 nanovectors to enhance tumor-specific accumulation. These peptides included one ligand targeting the angiogenic tumor neovasculature, one mitochondrion-directed apoptosis-inducing peptide, and one cell-penetrating peptide (CPP) with high potency and selectivity toward cancer cells.

Methods: Physicochemical characterization, cytotoxicity analysis, cellular uptake, regulation mechanisms, and *in vivo* studies on miR-200- and irinotecan-incorporated nanoparticles were performed to identify the potential antitumor efficacy and biosafety issues involved in HNC treatment and to elucidate the underlying signaling pathways.

Results: We found that the cleavable PEG layer responded to low extracellular pH, and that the CPP and targeting peptides were exposed to improve the uptake and release of miR-200 and irinotecan into HNC human tongue squamous carcinoma (SAS) cells. The apoptosis of SAS cells treated with the combinatorial therapy was significantly induced by regulating various pathways, such as the Wnt/β-catenin, MDR, and EMT pathways. The therapeutic efficacy and safety of the proposed co-treatment outperformed the commercially available Onivyde and other formulations used in a SAS tumor-bearing mouse model in this study.

Conclusion: Chemotherapy and gene therapy co-treatment involving pH-sensitive and targeting peptide-modified nanoparticles may be an innovative strategy for HNC treatment.

Key words: head and neck cancer, self-cleavable PEG-shell, combinatorial therapy, microRNA, pH-sensitive targeting nanoparticles

Introduction

Head and neck cancer (HNC) is one of the most significant causes of morbidity and mortality globally and has a poor treatment outcome [1]. Among HNCs, oral squamous cell carcinoma (OSCC), especially of the tongue, is one of the most diagnosed oral cancer phenotype [2]. Human tongue squamous carcinoma

(SAS) cells are notably highly aggressive, migratory, and invasive [3]. Thus, SAS cells were used in the present study to represent a tumor-progression model of OSCC [4]. Current HNC chemotherapeutic agents such as 5-fluorouracil and cisplatin have been considered standard treatments, but OSCC is frequently unresponsive to common chemotherapy and is usually accompanied by early relapse, distant metastasis, and poor prognosis [5]. Irinotecan (Iri), a camptothecin derivative, is a validated option in second- and third-line settings [6]. However, therapy resistance and unremarkable improvements have been observed in currently available chemotherapeutics [7]. Epithelial-to-mesenchymal transition (EMT), resistance to current chemotherapy, and systemic toxicity caused by available antineoplastic agents hinder the efficacy and safety of HNC treatment [8]. Iri, a topoisomerase (Topo)-I inhibitor, induces cell death by inhibiting the religation of double-strand DNA [9]. Iri and its metabolite SN-38 are typically pumped outside cancer cells by P-glycoprotein (P-gp) and multidrug resistance (MDR)-associated proteins (MRPs), leading to MDR [10]. EMT also contributes to the development of acquired Iri resistance and elevated migration and invasion in different cancer types [11,12]. However, the capacity of current HNC therapies to suppress MDR and EMT is limited [13]. Accordingly, identifying suitable gene therapeutics for co-treatment with Iri is urgent to effectively inhibit Iri resistance and increase the chemosensitivity of HNC to this drug.

MicroRNAs (miR), small noncoding RNAs of 18–25 base pairs, modulate mRNA expression at the post-transcriptional level [14]. EMT activation plays a critical role in tumor invasion and metastasis [15]. Thus, repressing EMT action as a potential anticancer strategy is very important. The overexpression of zinc finger E-box binding homeobox 1 (ZEB1) triggers EMT by suppressing miR-200 family members [16,17]. Accordingly, miR-200 family upregulation is critical to inhibit the expression levels of ZEB1 and ZEB2, thereby reducing EMT in OSCC [18]. Furthermore, the induction of the miR-200c-3p expression inhibits ZEB1 function and increases the sensitivity to target therapy (i.e., MEK inhibition) in KRAS mutation-resistant lung cancer [19]. Moreover, the downregulation of miR-200 family members plays a key role in the anti-apoptosis, progression, invasion, metastasis, and drug resistance of different cancers (e.g., OSCC, cervical cancer, pancreatic cancer, nasopharyngeal carcinoma, and soft-tissue sarcomas) [20]. Nevertheless, the use of miR-200 alone ineffectively suppresses tumors [16]. Thus, the administration of miR-200 in solid lipid nanoparticles (SLNs) and Iri in liposomes (Lip) may improve current clinical problems such as rapid degradation, limited tumor penetration, and low uptake into cancer cells, which are associated with chemo- and gene therapies [21]. The pretreatment of anionic miR-200 in cationic SLNs reportedly activates related signaling pathways such as EMT suppression to increase the cytotoxic potency of using Iri-loaded anionic Lip against colorectal cancer (CRC) in HCT116 cells and CRC-bearing mice [22].

SLN and Lip, which are decorated with cell-penetrating peptides (CPPs), show different characteristics in reducing nonselective cellular uptake and enhancing specific tumor targeting. CPPs are a group of short cationic peptides usually rich in arginine and lysine [23]. **N peptide** can bind to nerve/glial antigen 2 (NG2) overexpressed in the tumor neovasculature and thus functions as a targeting ligand [24]. Given the selectivity of the N peptide in tumor cells, it may serve as a prospective modification for the tumor-specific delivery of nanomedicines [24]. N peptide modification reportedly enhances nanoparticle internalization via the binding of N peptide to NG2 receptor, leading to effective antiangiogenic therapy [25]. **C peptide** displays high potency and selectivity against cancer cells, but it shows lower toxicity to normal cells than that of TAT peptide [26]. Interestingly, our pervious study has also indicated that the transport of gefitinib-encapsulated Lip modified with C peptide across the blood–brain barrier is improved by modulating the transcytosis pathway primarily via the adsorptive-mediated mechanism [27]. **M peptide**, a mitochondrion-localizing peptide, possesses pro-apoptotic KLA residues [28]. This peptide potentiates mitochondrion-mediated lung carcinoma cell death via membrane-potential reduction and ATP depletion [29]. M peptide-conjugated nanostructures also facilitate doxorubicin accumulation in mitochondria, thereby triggering the release of cytochrome c and increasing the expressions of caspase-9, caspase-3, p21, and p53 [30].

In the present study, the lipid core of SLNs and Lip is modified by N peptide for tumor targeting, M peptide for mitochondrion directing, and C peptide for enhanced cancer penetration to prepare **SLN-CMN** and **Lip-CMN**. Moreover, the PEG derivative O′-methyl polyethylene glycol (omPEG) was conjugated into lipid to form a pH-sensitive imine bond. SLN-CMN and Lip-CMN were then additionally modified with this cleavable long-chain PEG–lipid derivative (lipid-imine-omPEG) to prepare **omSLN-CMN** and **omLip-CMN** (Figure 1A). This design of two nanoparticles coated with multifunctional peptides and a PEG derivative

responsive to an acidic tumor environment may provide potential basis for the separate delivery of combinatorial therapy comprising Iri and miR-200. This strategy may increase passive tumor targeting via the enhanced permeability and retention (EPR) effect, intensify active tumor targeting through specific ligand–receptor binding, and improve endosomal escape and mitochondrial localization.

Materials and methods

Materials

FAM-miR-200 and has-miR-200c-3p were synthesized by GenePharma (Shanghai, China). Iri hydrochloride was purchased from AK Scientific (Union City, CA, USA). C, M, and N peptides were custom synthesized by Kelowna (Taiwan). Cholesterol and paraformaldehyde were bought from Acros (Geel, Antwerp, Belgium). All lipids were obtained from Avanti (Alabaster, AL, USA). Lipofectamine™ 3000 was procured from Thermo Fisher Scientific (Waltham, MA, USA). All cell culture media and reagents were bought from Gibco BRL (Grand Island, NY, USA). Most of the other chemical reagents were obtained from either Merck (Darmstadt, Germany) or Sigma–Aldrich (St. Louis, MO, USA).

Synthesis of 1,2-distearoyl-sn-glycero-3-phosphoethanolamine-omPEG

1,2-distearoyl-sn-glycero-3-phosphoethanolamin e (DSPE) was dispersed in chloroform/methanol (9:1), and omPEG was added to the solution. The mole ratio of DSPE and omPEG was 1:1. The mixture was allowed to react overnight at 50 °C. DSPE-omPEG was then obtained after the organic solvent was removed using a centrifugal evaporator (Genevac SF50, Genevac Ltd., Ipswich, England, UK). DSPE-omPEG was examined with ^{1}H NMR (400 MHz, Bruker Avance III, Rheinstetten, Germany) to confirm the structure of the conjugate.

Synthesis of peptide-conjugated lipid

DSPE-PEG-maleimide was dissolved in chloroform/methanol (9:1). C, M, and N peptides were added to the lipid solution (individual peptide/lipid molar ratio = 1:1) and allowed to react overnight. After evaporation, the residue was dissolved in water and dialyzed against water overnight to remove unconjugated peptides by using a dialysis bag (3.5–5 kDa membrane; Spectrum Laboratories, CA, USA). The final product (DSPE-PEG-peptide) was lyophilized, and the structure was verified through matrix-assisted laser desorption ionization time-of-flight mass spectrometry (MALDI-TOF MS; Applied Biosystems, MA, USA).

Preparation of peptide-conjugated and pH-sensitive Iri/omLip-CMN

Peptide-conjugated and Iri-loaded Lip (Iri/Lip-CMN) were prepared by thin-film hydration. The molar ratio of DSPC, cholesterol, DSPE-PEG-peptide, and DSPE-omPEG was 1:0.1:0.1:0.1. In a typical procedure, the above mixture at the indicated ratio was dissolved in chloroform/methanol (9:1). After the organic solvent was removed, the lipid thin film was suspended in phosphate-buffered saline (PBS) at 37 °C. The Lip were extruded through 400, 200, and 100 nm membrane filters. Iri was then added to blank Lip, and further incubation was performed at 50 °C for 1 h through an ammonium sulfate gradient method to obtain Iri-loaded Lip.

Preparation of peptide-conjugated and pH-sensitive miR/om SLN-CMN

SLN were prepared by dispersing L-α-phosphatidylcholine (PC), cholesterol, DOTAP, DSPE-PEG-peptide, and DSPE-omPEG at a molar ratio of 1:0.1:0.1:0.1:0.1 in methanol/dichloromethane. The above mixture was added dropwise into Tween 80 solution. A miR solution was loaded into the SLNs, and the final dispersion was maintained at room temperature for 30 min.

Characterization of various Lip and SLN formulations

The size distribution and zeta potential of Iri/omLip-CMN and miR/om SLN-CMN were determined using a Zetasizer Nano-ZS particle-size analyzer (Malvern Instruments Ltd., Malvern, Worcestershire, England, UK). The morphological characteristics of these formulations were imaged under a transmission electron microscopy (TEM) system (JEM-2000EXII, Japan). Morphology was further visualized using a cryo-TEM instrument (Tecnai G2 F20 TWIN, FEI Company, The Netherlands).

Encapsulation efficiency (EE%) and drug-loading capacity (DL%)

A dispersion of Iri- or miR-incorporated nanoparticles was centrifuged at 15 000 rpm and 4 °C by using an ultracentrifuge filter (Amicon®) for 30 min. The filtrate was collected and analyzed with an Ultrospec 8000 PC spectrophotometer (Biochrom Ltd., Cambridge, England, UK) and NanoDrop (Thermo Fisher, MA, USA). The collected nanoparticles were broken with 0.5% Triton X 100, and the residual nanoparticles were dissolved in methanol and chloroform after centrifuging at 15 000 rpm and 4 °C for 30 min. Iri or miR was analyzed as mentioned above. Each sample was detected in triplicate. The

EE% and DL% of Iri or miR in different formulations were computed using the following formulas:

$$EE\% = [(W_1 - W_2)/W_1] \times 100\%, \quad (1)$$

$$DL\% = [(W_1 - W_2)/W_3] \times 100\%, \quad (2)$$

where W_1 is the weight of the added Iri or miR, W_2 is the weight of Iri or miR in the filtrate, and W_3 is the weight of the total phospholipids.

Protection test of miR-loaded formulations via gel-retardation assay

miR was encapsulated with or without different SLN formulations (SLN, SLN-CMN, and omSLN-CMN) and incubated with 1% RNase or 50% fetal bovine serum (FBS) at 37 °C. The samples were loaded into the gel, run with polyacrylamide gel (PAGE) at 60 V, and stained with ethidium bromide at 25 °C for 30 min. Afterwards, the gel was monitored and scanned using a gel-documentation system (DigiGel, TopBio, Taipei, Taiwan).

Changes in pH-induced size and zeta potential

Changes in the pH-sensitive size and zeta potential of Lip-CMN and SLN-CMN with or without pH-sensitive omPEG or PEG layer (no imine bond for comparison) were detected using Malvern Zetasizer Nano ZS90. These nanoparticles were incubated in PBS (pH 7.4 and 5.5) at 25 °C for 1 h. The size and zeta potential of each sample were measured in triplicate.

In vitro pH-sensitive release

To verify the pH-sensitive drug release, different Iri- or miR-encapsulated preparations were maintained in a dialysis bag (1000–3500 MWCO) and dialyzed sequentially against PBS at pH 7.4 and 6.5 at 37 °C. At the designated time (0, 1, 2, 5, 8, 12, 24, 48, and 72 h), samples were withdrawn from the medium and substituted with an equal volume of fresh medium. Iri- or miR concentrations were detected using a spectrophotometer as mentioned above to calculate the cumulative drug-release percentage.

Cell lines

SAS and SAS/luc cells, obtained from Professor Muh-Hwa Yang's lab, were cultured in Dulbecco's modified Eagle's medium (DMEM) supplemented with 10% FBS. Normal oral keratinocyte (NOK) cells were cultured in DMEM with 10% FBS, 100 IU/mL penicillin, and 100 mg/mL streptomycin.

pH-sensitive cellular uptake

The cellular uptake of SAS and NOK cells was quantified by flow cytometry. The cells were treated with various formulations incorporating daunorubicin (DNR; a fluorescent probe for Iri), and the collected cell pellets were washed with 1 mL of cold PBS and re-suspended in PBS (pH 7.4) for NOK and PBS (pH 7.4 and 6.5) for SAS. The fluorescence intensity of DNR uptaken by the cells was measured with a FACSCalibur flow cytometer (BD Biosciences, San Jose, CA, USA).

Transfection study

Various FAM-miR-200 formulations were added to SAS cells, and the mixtures were incubated for 24 h. The cell pellets were centrifuged, collected, and washed with 1 mL of cold PBS. The fluorescence intensity of FAM-miR-200 that entered the cells was detected through flow cytometry and compared with that of commercially available transfection agents, such as T-Pro, Viromer, and Lipofectamine 3000.

Identification of cellular-uptake pathways

SAS cells were preincubated with different endocytosis inhibitors at 37 °C for 1 h. The endocytosis inhibitors included 5-(N,N-dimethyl) amiloride (DMA), nystatin, chlopromazine (CPZ), poly-L-lysine, and methyl-β-cyclodextrin (MBCD). After incubating the cells with DNR/Lip-CMN and FAM-miR/SLN-CMN for another 3 h, the resulting cell pellets were harvested and washed with cold PBS. Fluorescence intensity was then determined using a flow cytometer.

Identification of intracellular localization

SAS cells were seeded, incubated with DNR/Lip-CMN or FAM-miR/SLN-CMN, fixed with 4% paraformaldehyde for 10 min, and stained with MitoTracker® Green (MitoGreen) or MitoTracker® Red (MitoRed) to monitor mitochondrial localization. NG2 was identified by immunofluorescence staining with cyan-labeled anti-NG2 antibody overnight. The cells were stained with DAPI at 37 °C to locate the nucleus. Images were taken using a confocal laser scanning microscopy (CLSM) instrument (Olympus FV10i).

Cell-viability evaluation by sulforhodamine B (SRB) assay

NOK or SAS cells were seeded in 96-well plates overnight. The cells were pretreated with miR-200 formulations for 24 h and then treated with various Iri formulations for 24 h at 37 °C. Cell viability was measured by SRB assay. Afterwards, 0.04% SRB was added to the individual well for 10 min, and each well was washed thrice with 1% acetic acid. The wells were dried at room temperature for 24 h, and then 10 mM Tris base was added to each well. Absorbance was detected at 540 nm by using a microplate TECAN reader.

Annexin V–propidium iodide (PI) assay

The cells were treated with six formulations, namely, control (CTR), Iri, Iri/Lip, Iri/Lip-CMN, miR-200/SLN-CMN, and miR-200/SLN-CMN+Iri/Lip-CMN, for 48 h. To determine the percentage of cell populations in apoptosis, necrosis, and death, the harvested cells were washed and stained with Annexin V–PI labeling solution in darkness. The apoptosis, necrosis, and death (%) of SAS cells were monitored and computed using a BD flow cytometer.

Western blot assay

SAS cells were seeded, incubated with the above-mentioned six formulations for 24 h, and lysed through radioimmunoprecipitation assay. Proteins were examined by BCA protein assay. Protein samples were separated by SDS-PAGE and transferred onto polyvinylidene difluoride membranes. After blocking the membranes via nonspecific binding with 5% nonfat milk for 1 h, blots were incubated with primary antibodies against various proteins from Cell Signaling or Abcam at 4 °C overnight and conjugated with horseradish peroxidase-linked immunoglobulin G (Jackson). After being developed in a Millipore detection system and reprobed with anti-β-actin antibody, these blots were visualized with enhanced chemiluminescence kits (PerkinElmer).

Migration assay

SAS cells were seeded in inserts (Ibidi GmbH, Munich, Germany), treated with the different formulations, and monitored for 15 h. Images were obtained through optical microscopy, and the migration area was quantified using Image J. Relative migration percentages were calculated using the following equation:

$$\text{Relative migration area (\% of area at 0 h)} = 100\% - [\text{blank area}_{(15h)}/\text{blank area}_{(0h)} \times 100\%]. \quad (3)$$

Establishment of *in vivo* SAS-tumor bearing mouse model

Male BALB/c nude (nu/nu) mice (6 weeks old; ~22 g body weight) were purchased from the National Laboratory Animal Center and maintained in the Animal Center of National Yang-Ming University. Animal care and handling procedures were in accordance with the guidelines approved by the Institutional Animal Care and Use Committee. SAS-luc cells were injected subcutaneously into the right cheek region of the mice. Tumor size was calculated as follows:

$$V = (L \times W^2)/2 \quad (4)$$

where L is the longest diameter (mm), and W is the shortest diameter (mm) perpendicular to the longest axis.

Antitumor efficacy, body weight, and IVIS imaging evaluation of SAS tumor-bearing mice

Tumors were allowed to grow to approximately 60 mm^3 before treatment. SAS/luc tumor-bearing mice were randomly divided into eight groups (n = 5; Iri = 40 mg/kg; miR-200 = 1.25 mg/kg): 1) saline (control, CTR); 2) Iri; 3) Iri/Lip; 4) Iri/Lip-CMN; 5) miR-200/SLN-CMN + Iri/Lip-CMN; 6) Iri/omLip-CMN, miR-200/omSLN-CMN + Iri/omLip-CMN; 7) Onivyde; and 8) miR-200/omSLN-CMN + Onivyde [22,31]. For the combined treatment of miR-200 and Iri formulations, after treatment with miR-200/SLN-CMN for 24 h, various Iri formulations were administered. Each group received different formulations on the 1st and 14th days. The tumor size and body weight of the mice were measured with a digital caliper every 2 days after treatments, and tumor volume (V) was computed according to Equation 4. Fluorescence images were visualized with IVIS Spectrum (PerkinElmer, Waltham, MA, USA) 1 day after the final treatment. Survival percentage was calculated as the survival number of mice at the indicated time divided by the initial number of mice.

Biodistribution, biochemical tests, and hematoxylin and eosin (H&E) staining

After 48 h of the final treatment, 170 μL of blood samples was obtained from the orbital sinus of mice. After centrifugation, the serum levels of glutamate pyruvate transaminase (GPT), creatinine (CRE), and creatine kinase-MB (CK-MB) were detected using the corresponding activity assay kits (Fujifilm, Tokyo, Japan) in a clinical dry-chemistry analyzer (Fuji Dri-Chem 7000 V, Fujifilm Corp.) to evaluate liver, kidney, and heart functions.

After the mice were sacrificed, their liver, kidney, intestine, and tumor tissues were preserved in 4% formaldehyde and embedded in paraffin for H&E staining. The tissue samples were collected, frozen rapidly in liquid nitrogen, and stored at −80 °C. A tissue size of approximately 100 mg was transferred into a glass vial. The tissues were disrupted by manual grinding with a mortar and pestle. After adding methanol and water to extract Iri from the tissues, the samples were vortexed and centrifuged at 3000 rpm and 4 °C. The upper layer of each sample was transferred into separate glass vials, and the amount of Iri was analyzed with an Ultrospec 8000 PC spectrophotometer (Biochrom Ltd., Cambridge, England, UK).

Table 1. Characterization of various Lip and SLN formulations

Formulations	Particle size (nm)	PDI	Zeta potential (mV)	Encapsulation; efficiency (%)	Drug-loading; capacity (%)
Lip	164.8 ± 3.41	0.17 ± 0.02	-9.17 ± 1.68	–	–
Lip-CMN	166.3 ± 3.11	0.13 ± 0.05	-8.21 ± 1.19	–	–
omLip-CMN	170.2 ± 1.26	0.15 ± 0.04	-9.88 ± 1.42	–	–
Iri/Lip-CMN	172.1 ± 2.34	0.17 ± 0.05	-7.23 ± 1.26	85.89 ± 2.18	18.79 ± 1.22
Iri/omLip-CMN	175.2 ± 2.27	0.16 ± 0.04	-8.18 ± 1.43	86.28 ± 2.29	19.88 ± 1.03
SLN	133.8 ± 1.65	0.16 ± 0.07	20.47 ± 2.21	–	–
SLN-CMN	136.7 ± 2.25	0.21 ± 0.05	22.15 ± 1.25	–	–
omSLN-CMN	139.9 ± 2.76	0.18 ± 0.04	18.20 ± 1.49	–	–
miR-200/SLN-CMN	143.1 ± 1.18	0.19 ± 0.04	17.88 ± 1.38	86.78 ± 0.56	18.34 ± 1.23
miR-200/omSLN-CMN	148.6 ± 0.36	0.12 ± 0.05	16.70 ± 1.69	87.19 ± 0.81	19.52 ± 1.56

Terminal deoxynucleotidyl transferase dUTP nick end labeling assay (TUNEL)

TUNEL assay was carried out to examine *in vivo* apoptosis induction in the tumor tissues and vessels of SAS-bearing mice. In a typical procedure, tumor and vessel samples were collected, frozen, and fixed with 4% paraformaldehyde for 20 min. The samples were mixed with a solution of an in situ cell death detection kit (Roche, Germany) in accordance with the manufacturer's instruction. Afterwards, the final products were stained with nuclear Hoechst dye for comparison and observed by CLSM.

Statistical analysis

Experimental data were expressed as the mean ± standard deviation. Statistical significance was analyzed with Student's t-test to compare the differences between the two treatment groups. Statistical analysis was also carried out using one-way ANOVA and Dunnett's multiple comparison tests. Differences at *P < 0.05, **P < 0.01, and ***P < 0.001 were considered statistically significant.

Results and discussion

Characterization of miR-200/omSLN-CMN and Iri/omLip-CMN

The imine bond of DSPE-omPEG successfully formed as confirmed by the peak at 9.35 ppm in the ^{1}H NMR spectra (Figure S1A). The conjugation of N, M, and C peptides with DSPE-PEG was verified through MALDI-TOF MS (Figures S1B–E).

The size, zeta potential, polydispersity index (PDI), EE%, and DL% of SLN and Lip with or without omPEG and CMN modification are summarized in Table 1. The mean diameters of miR-200/omSLN-CMN and Iri/omLip-CMN were 148.6 ± 0.36 and 175.2 ± 2.27 nm (Figures 1B–D), respectively, with a PDI of approximately 0.1–0.2. The zeta potentials of miR-200/omSLN-CMN and Iri/omLip-CMN were 16.70 ± 1.69 and -8.18 ± 1.43 mV (Figures 1C–E), respectively. Table 1 also shows the high EE% (>85%) and acceptable DL% of omLip-CMN and omSLN-CMN. Meanwhile, TEM and cryo-TEM were performed to investigate the morphological characteristics of miR-200/omSLN-CMN and Iri/omLip-CMN, and the results are shown in Figures 1F–H. The cryo-TEM image revealed that the om-PEG shell was coated around the Iri-loaded nanoparticle formulation, displaying the traditional bilayer structure of Lip with enclosed Iri crystals in the core (Figure 1H). Moreover, the miR protective features of different nanoparticle formulations were assessed. Results showed that omSLN-CMN completely prevented miR from degradation under the extreme condition of 50% FBS (Figure S2A). This finding suggested the necessity of this pH-sensitive imine bond in enhancing miR-protection ability. omSLN-CMN may have compacted miR into a condensed structure and thus prevented its degradation by nuclease. Additionally, more than 97% of Iri or miR were released from Iri or miR solution within the first 1 h, and the release percentage approached 100% within 12 h as indicated by the 72 h release profiles of Iri or miR at 37 °C (Figures S3A–B). Nevertheless, the percentages of Iri and miR released from omLip-CMN and omSLN-CMN at pH 7.4 were 55.85% ± 1.75% and 58.52% ± 1.99%, respectively, up to 72 h (Figures S3A–B), thereby verifying the limited release property of omLip-CMN and omSLN-CMN at physiological pH. Remarkably, at pH 6.5, the release percentage of Iri and miR from omLip-CMN and omSLN-CMN increased to 75.75% ± 2.11% and 80.29% ± 1.87%, respectively, at 72 h (Figures S3A–B). This finding confirmed the pH-responsive release characteristics of omLip-CMN and omSLN-CMN in acidic pH.

pH-sensitive characteristics of omLip-CMN and omSLN-CMN at pH 7.4 and 6.5

The pH-responsive changes in the size, PDI, and zeta potential of miR-200/omSLN-CMN and Iri/omLip-CMN at pH 7.4 and 6.5 are displayed in Figures 2A–B and S2B–E. Interestingly, after miR-200/omSLN-CMN were incubated with PBS (pH 6.5) for 30 min, another peak of the de-shedded omPEG layer with large particle size (Figure S2B). After de-coating, the zeta potential of the major peak increased

to 18.79 ± 8.12 mV, with a smaller separate peak at approximately -5 mV (Figures 2B and S2C). The particle sizes and zeta potentials of Iri/omLip-CMN at pH 7.4 and 6.5 also exhibited similar trends (Figures 2A–B and S2D–E). These findings revealed the removal of the DSPE-omPEG layer in the acidic tumor microenvironment to expose the cationic peptide-modified SLN-CMN and the less negatively charged Lip-CMN (compared with omLip-CMN). For comparison, we also prepared nanoparticles using DSPE-PEG5000 without an imine bond (Iri/PEG-Lip-CMN; the last two items in Figures 2A–B). The zeta potential of Iri/PEG-Lip-CMN at both pH 6.5 and 7.4 were similar to that of Iri/omLip-CMN at pH 7.4. By contrast, Iri/PEG-Lip-CMN at pH 6.5 showed slightly larger particle sizes than did Iri/PEG-Lip-CMN at pH 7.4, suggesting the absence of pH-dependent de-shielding of the PEG layer for Iri/PEG-Lip-CMN (Figures 2A–B).

The effects of different pH conditions on the uptake of DNR (as a probe of Iri) incorporated into different formulations were examined in noncancerous NOK cells and HNC SAS cells through flow cytometry. Results showed that the fluorescence intensities of DNR in NOK (Figure 2C) and SAS (Figure 2D) cells delivered by omLip-CMN were much lower than those delivered by Lip-CMN at pH 7.4, suggesting the excellent prevention of chemotherapeutics from being uptaken into normal and cancer cells by the om-PEG layer coating. These results also indicated the low intracellular accumulation of anticancer drugs delivered by omLip-CMN at physiological pH. However, the hydrolysis of the imine bond in omLip-CMN at pH 6.5 caused the exposure of the CMN-peptides modified on the surface of Lip-CMN, which remarkably increased the cellular uptake of DNR at pH 6.5 (Figure 2E). This result suggested that omLip-CMN may have prevented the entrance of the chemotherapeutic agent into normal cells (pH 7.4) and enhanced their pH-responsive uptake in the acidic tumor site (pH 6.5). This finding was consistent with our previous study using pH-sensitive nanoparticles [22]. Li et al. also reported the design of pH-sensitive boronate esters to release the chemotherapeutic agent bortezomib in a covalently assembled dopamine nanocarrier [32]. Fan et al. further used a pH-sensitive PEG shell de-coated from the inner core at the tumor site; they found increased cellular accumulation and fast release of fluorescence probe within the tumor cells, as well as enhanced photodynamic-therapy efficacy [33].

Mechanisms of cellular internalization and endosomal escape

Naked miR has short circulation time and limited intracellular accumulation at tumor sites because of rapid degradation by nucleases and poor endosomal escape [34]. Thus, we developed SLN-CMN to deliver miR-200 in SAS cells. As shown in Figure 3A, the relative transfection percentage of FAM-miR-200 by SLN-CMN was higher than that of common transfection reagents, including T-pro, Viromer® BLUE, and Lipofectamine™ 3000. This finding revealed the superior transfection enhancement of SLN-CMN primarily owing to the characteristic SLN design and specific modification of SLN by ligand N, CPP C, and mitochondrion-directing peptide M.

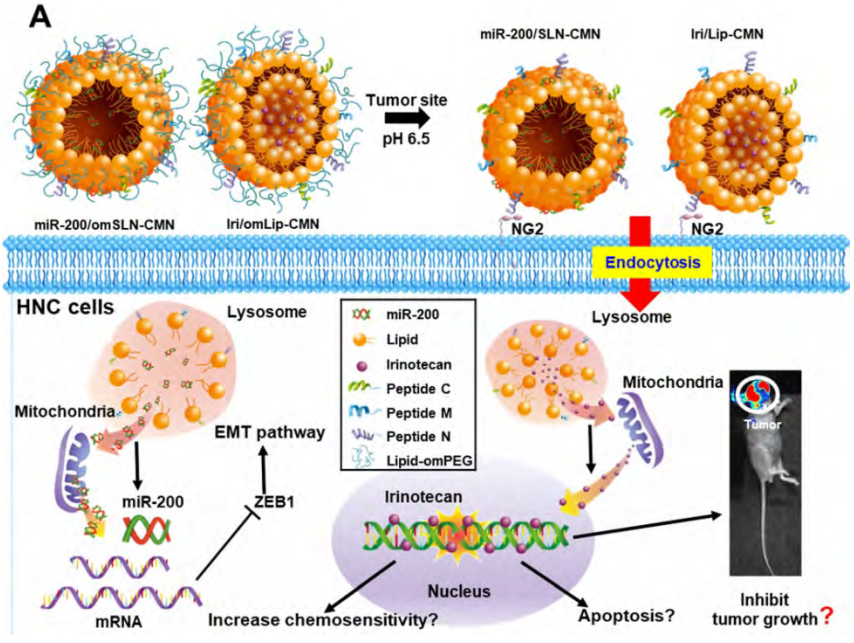

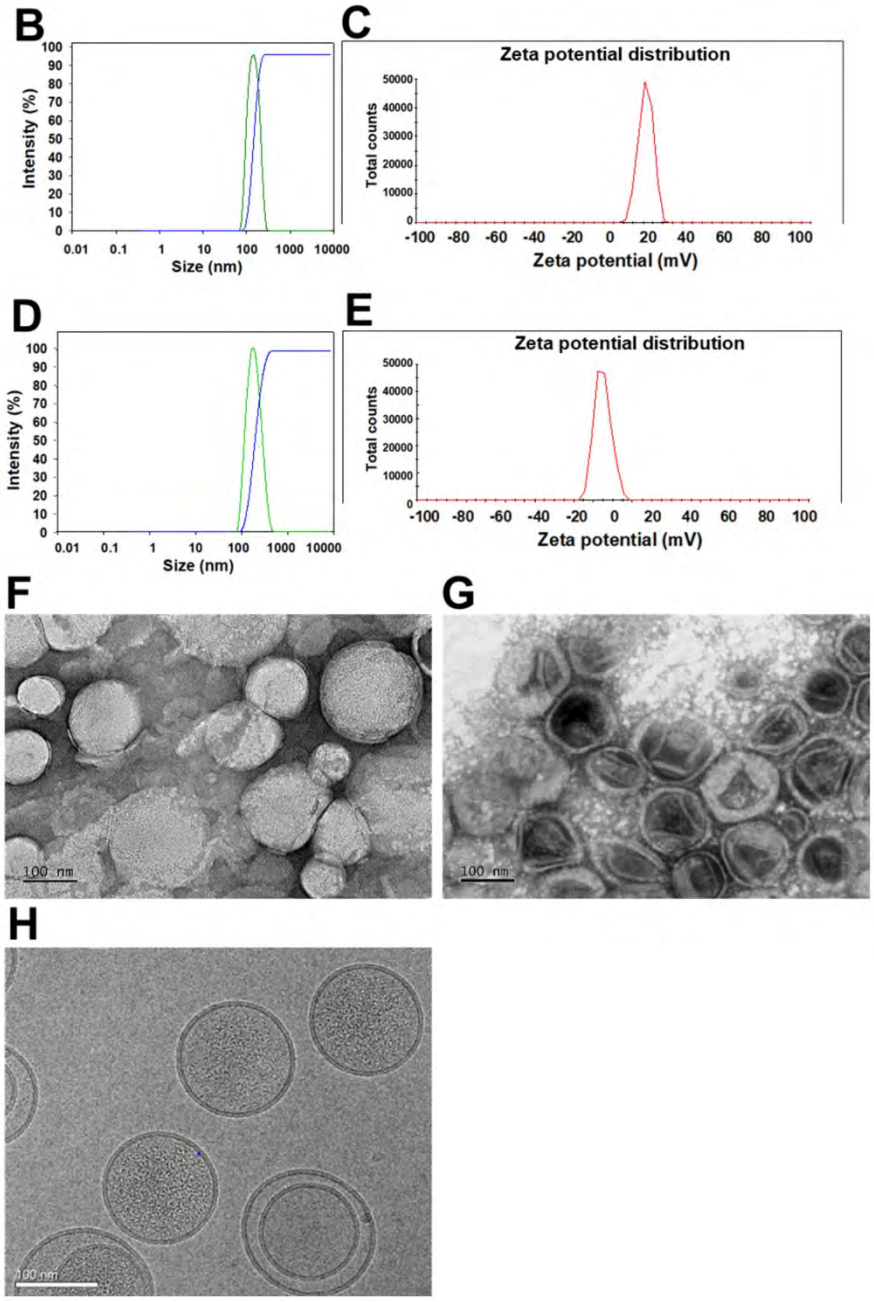

Figure 1. (A) Scheme of the rationale of pH-sensitive and peptide-modified liposomes (Lip) and solid lipid nanoparticles (SLN) incorporating irinotecan (Iri) and miR-200, respectively. (B–G) Sizes and zeta potential of (B–C) omSLN-CMN and (D–E) omLip-CMN were measured with Malvern Zetasizer. TEM images of (F) miR-200/omSLN-CMN and (G) Iri/omLip-CMN were observed using JEM-2000EXII TEM. (H) Cryo-TEM images of Iri/omLip-CMN. Bar = 100 nm. For each group, $n = 3$.

Nanoparticles are transported across the cell membrane via endocytic pathways [35], such as macropinocytosis and clathrin- and caveolae-dependent endocytosis [36]. Thus, we used different endocytosis inhibitors to block the internalization pathways in the present study. The cellular internalization inhibitors included DMA (macropinocytosis inhibitor), nystatin (caveolae-mediated endocytosis inhibitor), CPZ (clathrin-mediated endocytosis inhibitor), poly-L-lysine (adsorptive-mediated endocytosis inhibitor), and MBCD (cholesterol-dependent membrane fusion inhibitor). As shown in Figure 3B, SLN-CMN preferred to cross the cell membrane through macropinocytosis, adsorptive- and caveolae-mediated endocytosis. Nonetheless, clathrin- and adsorptive-mediated endocytosis were the two major pathways of Lip-CMN (Figure 3C). Although the surface modification of SLN-CMN and Lip-CMN by the cationic peptides C, M, and N allowed these two nanomedicines to be internalized by adsorptive-mediated endocytosis into SAS cells, SLN-CMN and Lip-CMN apparently displayed different internalization mechanisms.

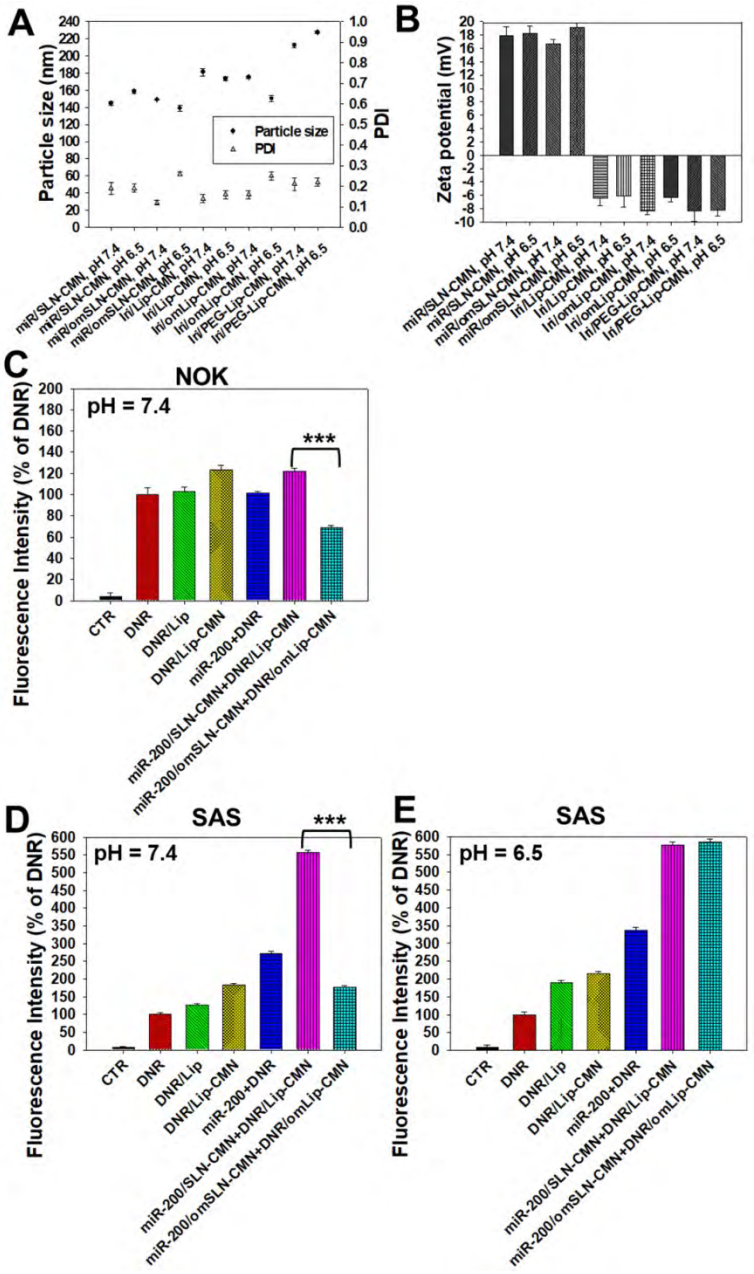

Figure 2. Changes in the pH-sensitive particle size, zeta potential, and cellular uptake of miR-200 and/or Iri formulations at pH 7.4 and 6.5. Changes in (A) sizes, PDI, and (B) zeta potential of miR-200 and/or Iri formulations were measured using a Zetasizer at 30 min after incubation with PBS at pH 7.4 or 6.5. (C–E) Cellular uptake of daunorubicin (DNR; a probe of irinotecan) in various formulations into (C) NOK cells at pH 7.4 and SAS cells at (D) pH 7.4 and (E) 6.5 for 24 h, as detected by flow cytometry.

Endosomal escape is an important step for the successful delivery of nanoparticles to intracellular targets [37]. The intracellular trafficking of internalized DNR/Lip-CMN and FAM-miR-200/SLN-CMN was observed by CLSM (Figures 3C–D). The DNR/Lip-CMN fluorescence (red) was co-localized with NG2 (stained with cyan-labeled anti-NG2 antibody) in SAS cells after 30 min of incubation. At 30 min, DNR/Lip-CMN was also co-localized with mitochondria (stained with MitoTracker as green; MitoGreen), which are typically located close to the nuclei. Particularly, DNR from Lip-CMN was predominantly co-localized with nuclei at 8 h, suggesting successful escape from the endosomes and/or lysosomes to its intracellular target (Figure 3D). For comparison, the trafficking of untargeted Lip and single-peptide-modified Lip was also investigated, and the results are shown in Figures S4A–D. We found that DNR/Lip-C enhanced Lip penetration into SAS cells to release DNR intracellularly (Figure S4B). DNR/Lip-M, with the mitochondrion-targeted peptide M, was verified to successfully transport DNR to mitochondria (Figure S4C) and thus activate the mitochondrion-associated apoptosis pathway (as shown below). The similar pro-apoptosis effect of M-peptide-linked

nanostructures has also been reported to induce the mitochondrion-mediated apoptosis and intensify the anticancer efficacy of doxorubicin *in vitro* [30]. Furthermore, the CLSM images confirmed that DNR/Lip-N was co-localized in SAS cells with NG2, a proteoglycan overexpressed in angiogenetic tumor cells (Figure S4D).

Additionally, FAM-miR-200/SLN-CMN (green) was co-localized mostly with NG2 of SAS cells at 10 min (Figure 3E). At 30 min, FAM-miR-200/SLN-CMN was distributed predominantly in the cytoplasm. Interestingly, FAM-miR-200 displayed an escalated extent of co-localization in mitochondria (stained with MitoRed) at 3 h (Figure 3E) at least partially because N peptide is a ligand that targets mitochondria. These results showed that SLN-CMN had good endosomal-escape capability and high accumulation in mitochondria and cytoplasm, thereby preventing miR-200 degradation in early endosomes and lysosomes.

Toxicity to noncancerous and cancer cells

All SLN formulations in the presence or absence of miR-200 showed marginal toxicity to NOK cells (Figure 4A) as measured by SRB assay. The Iri solution displayed approximately 40% cytotoxicity to noncancerous NOK cells, but the toxicity of Iri/Lip, Iri/Lip-CMN, and Iri/omLip-CMN to NOK cells was lower than that of Iri solution (Figure 4A). The combined treatment of Iri/omLip-CMN and miR-200/omSLN-CMN did not increase the cytotoxicity to NOK cells (Figure 4A). This result suggested that these liposomal Iri formulations may diminish the possible Iri-induced side effects, such as oral mucositis, nausea, and vomiting [38]. Iri and/or miR-200 in different formulations showed various cytotoxic effects on SAS cells, as observed by SRB assay (Figure 4B). We found that the initial administration of miR-200/SLN-CMN followed by Iri/Lip-CMN caused a significant reduction in cancer-cell viability (about 55% inhibition; Figures 4B and S5). The co-administration of miR-200 and Iri in one formulation such as SLN-CMN or Lip-CMN exhibited mild cytotoxicity on SAS cells (15%–20% inhibition on SAS cell viability; Figure S5). The simultaneous co-treatment of miR-200/SLN-CMN and Iri/Lip-CMN showed approximately 30% inhibition on SAS cells (Figure S5). Remarkably, the greatest growth inhibition of SAS cells (about 60% inhibition; Figure 4B) was found in the initial treatment with miR-200/omSLN-CMN followed by Iri/omLip-CMN formulation. These results indicated the necessity to pretreat SAS cells with miR-200/omSLN-CMN for 24 h to activate the critical anticancer signaling pathways (as verified below) and thus further enhance the cytotoxic effect of Iri/omLip-CMN on SAS cells (Figures 4B and S5).

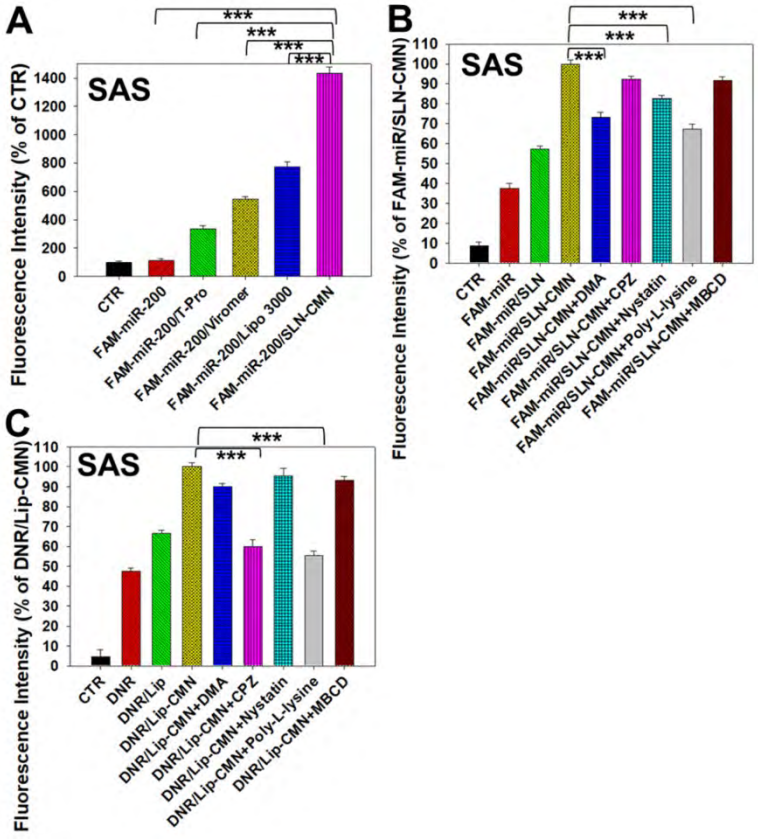

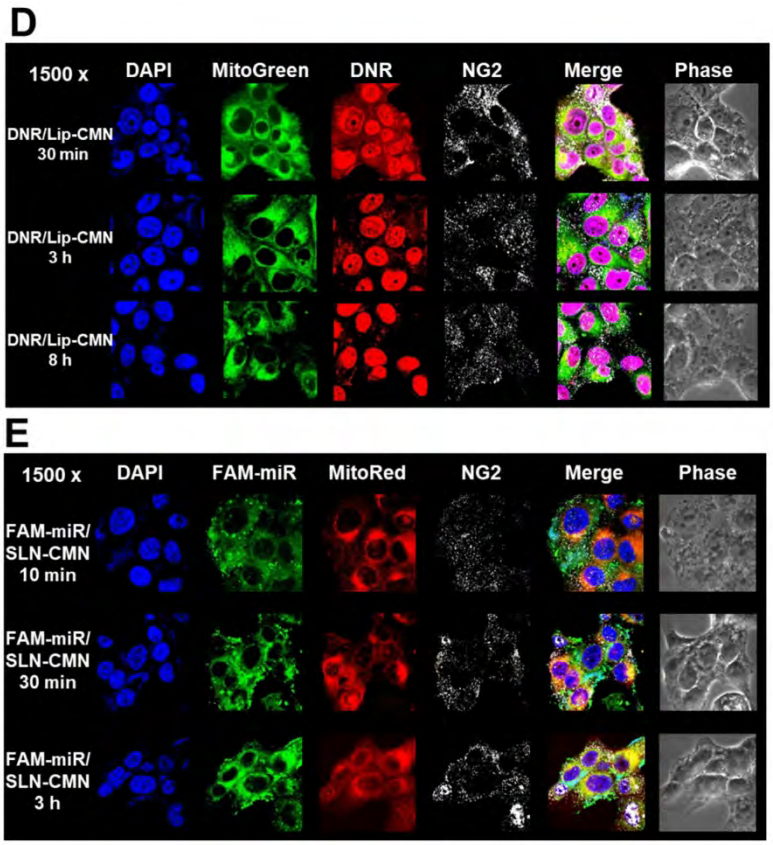

Figure 3. Transfection, cellular internalization, and intracellular trafficking of various miR-200 formulations in SAS cells. (A) Flow cytometry of the transfection efficiency (%) of FAM-miR-200 in the presence of different transfection reagents for 24 h. FAM-miR-200/Lipo 3000: FAM-miR-200/Lipofectamine 3000. (B) Endocytosis mechanisms of FAM-miR-200/SLN-CMN in SAS cells were detected by incubating the cells with specific endocytosis inhibitors at 37 °C for 1 h. Then, the cells were treated with FAM-miR formulations for another 3 h. The endocytosis inhibitors included 5-(N,N-dimethyl) amiloride (DMA), nystatin, chlopromazine (CPZ), poly-L-lysine, and methyl-β-cyclodextrin (MBCD). ***$P < 0.001$ compared with FAM-miR-200/SLN-CMN without the inhibitor. (C) After treatment with the above endocytosis inhibitors for 1 h at 37 °C, the cells were treated with different DNR formulations for another 3 h. ***$P < 0.001$ compared with DNR/Lip-CMN without the inhibitor. (D) DNR/Lip-CMN was added to the cells for 30 min, 3 h, and 8 h. Intracellular localization in SAS cells was observed through CLSM. Blue: DAPI (a nuclear dye); green: MitoGreen (MitoTracker Green; a mitochondrial dye); red: DNR; Gray: NG2 (nerve/glial antigen 2). (E) FAM-miR-200/SLN-CMN was added to the cells for 10 min, 30 min, and 3 h. Intracellular trafficking was observed by CLSM in SAS cells. Blue: DAPI; green: FAM-miR200; red: MitoRed (MitoTracker Red; a mitochondrial dye); gray: NG2.

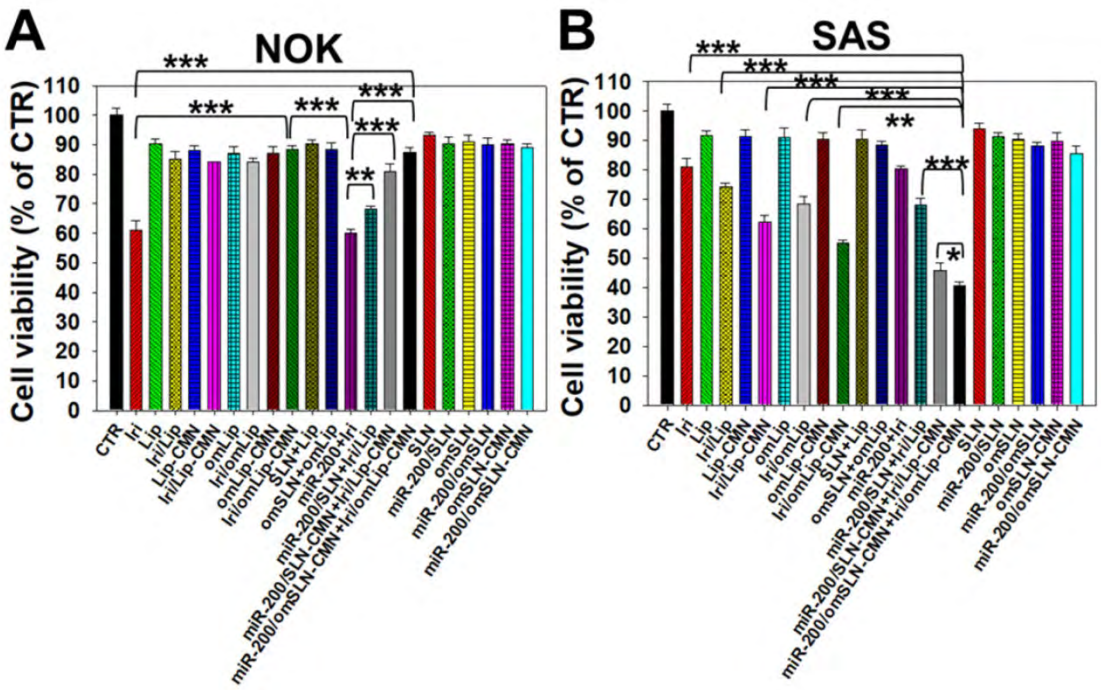

Figure 4. Cytotoxicity of various formulations on NOK and SAS cells. (A) NOK cells and (B) SAS cells were treated with different formulations (SAS = 0.7 μM; miR-200 = 100 nM) for 48 h, and cell viability was determined by SRB assay (*statistical significance at $P < 0.05$; ** $P < 0.01$; *** $P < 0.001$).

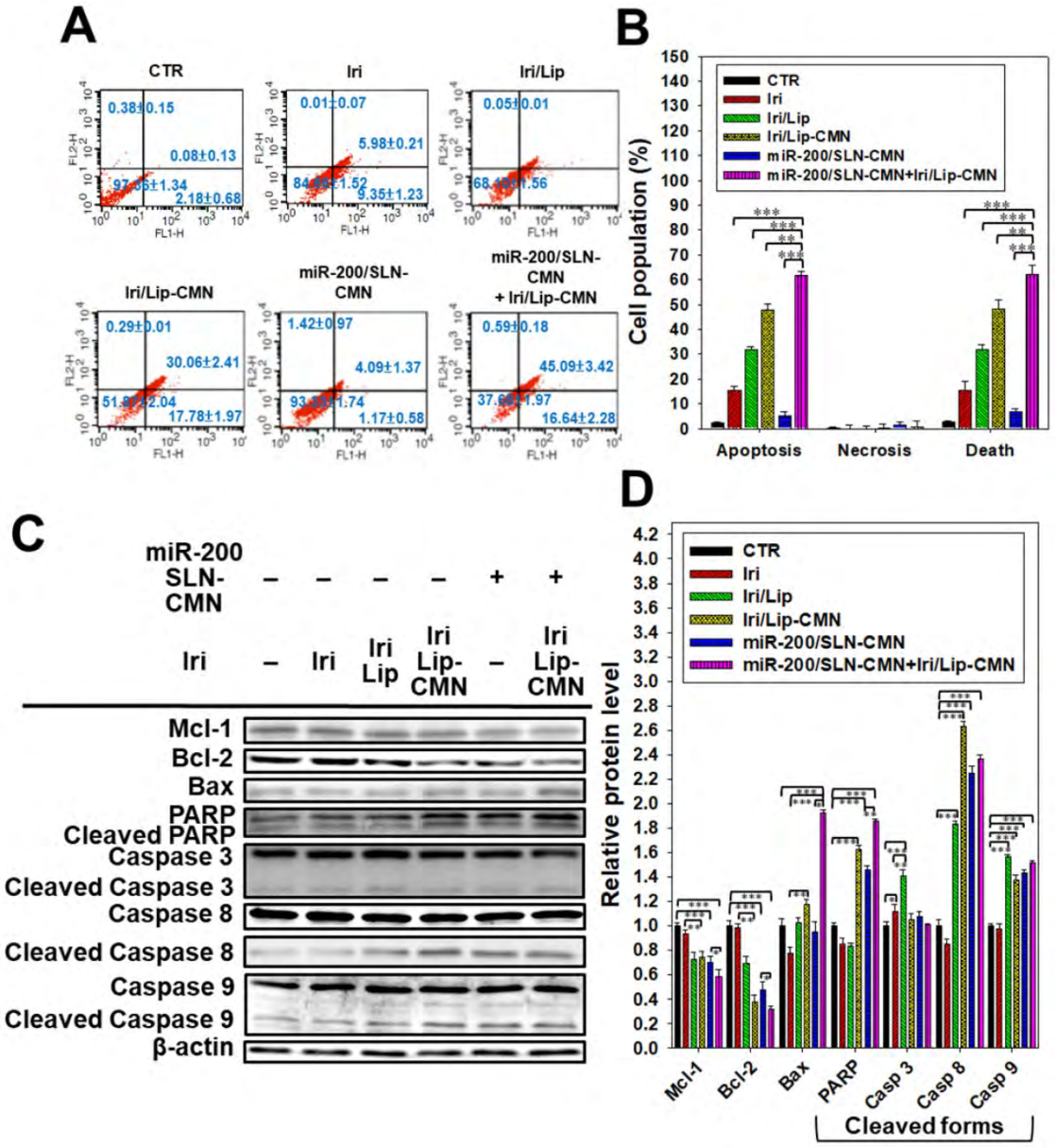

Figure 5. Anticancer effect of different formulations on the apoptosis pathway in SAS cells. (A) SAS cells were pretreated with miR-200/SLN-CMN (100 nM) for 24 h and then treated with irinotecan (Iri) or Iri/Lip-CMN (SAS = 0.7 μM) for 48 h. (B) Annexin V kit was used to detect and quantify the percentage of apoptotic cells (*statistical significance at $P < 0.05$; **$P < 0.01$; ***$P < 0.001$). (C–D) SAS cells were pretreated with miR-200/SLN-CMN (100 nM) for 24 h and then treated with Iri or Iri/Lip-CMN (SAS = 0.7 μM) for 48 h. Western blot assay was used to measure the protein levels on the apoptosis-associated pathway.

Enhanced apoptosis and related death mechanisms induced by the combined treatment in SAS cells

Iri causes cancer cell death by inhibiting Topo-I through the formation of stable Topo-I–DNA complexes [39]. Its combined treatment with miR-200/SLN-CMN further exacerbated the apoptosis effects of Iri/Lip-CMN against SAS cells (Figures 5A–B). Our molecular-mechanism investigation by Western blotting indicated that after treatment with miR-200/SLN-CMN and Iri/Lip-CMN, the protein expression levels of Bax, cleaved PARP, and caspases 8 and 9 were remarkably upregulated, whereas the protein expression levels of Bcl-2 and Mcl-1 were considerably downregulated (Figures 5C–D). These results confirmed that Iri was an apoptosis inducer [9]. The encapsulation in peptide-modified Lip (Iri/Lip-CMN) and the combined treatment with miR-200/SLN-CMN potentiated the ability of Iri to activate apoptosis. Lip-CMN or SLN-CMN may have enhanced the transport of Iri and/or miR 200 to mitochondria or the neighboring environment to activate the mitochondrion-related intrinsic apoptosis pathway and induce the extrinsic apoptosis pathway (Figure 5).

miR-200/SLN-CMN as a migration inhibitor and chemotherapeutic sensitizer in SAS cells

miR-200 inhibits cancer-cell migration and invasion by targeting ZEB1 and 2 [18]. EMT, a crucial tumor-progression factor, promotes the exacerbation of metastasis, which is one of the major causes of cancer-associated death in patients [40]. Furthermore, the Wnt/β-catenin signaling pathway is critical to the regulation of cell proliferation, differentiation, adhesion, resistance, and migration [41]. The MDR pathway also plays an important role in drug resistance and treatment failure [42]. MDR1 or ATP-binding cassette subfamily B member 1 (ABCB1; P-gp) and other MDR genes, such as ABCC1 (MRP1) and ABCC2 (MRP2), are at least partially regulated by the TCF4/β-catenin transcriptional complex and the associated β-catenin signaling pathway [43,44]. The development of the EMT pathway required for metastasis is also related to the activated Wnt/β-catenin signaling pathway [45]. For example, slug, snail, and vimentin are regulated not only by the EMT pathway but also by the β-catenin pathway [46]. As shown in Figures 6A–B, the protein expression levels of p-GKS-3β, β-catenin, Cyclin D1, and c-Myc were markedly downregulated by miR-200/SLN-CMN. Furthermore, the combined treatment of miR-200/SLN-CMN and Iri/Lip-CMN demonstrated the highest inhibition (%) on these proteins. Interestingly, the protein expression levels of P-gp, MRP1, and MRP2 were also significantly inhibited when SAS cells were co-treated with miR-200/SLN-CMN and Iri/Lip-CMN (Figures 6C–D). As a result, miR-200 in SLN-CMN served as a chemotherapy sensitizer in SAS cells to increase the cytotoxicity of Iri loaded in Lip-CMN. Accordingly, the protein expression levels of E-cadherin (an epithelial marker) were enhanced, but those of various transcription factors such as ZEB1, slug, snail, and vimentin (mesenchymal markers) were considerably reduced by the combined treatment of miR-200/SLN-CMN and Iri/Lip-CMN (Figures 6E–F). The migration of cells treated with Iri/Lip-CMN was inhibited after 15 h of treatment (Figures 6G–H). Importantly, the combined treatment of miR-200/SLN-CMN and Iri/Lip-CMN further potentiated the extent of inhibition (Figures 6G–H). These findings suggested that the combined treatment of miR-200/SLN-CMN and Iri/Lip-CMN considerably repressed the EMT, MDR, and Wnt/β-catenin signaling pathways (Figures 6A–H). Collectively, our results indicated that miR-200 in SLN-CMN may modulate multiple pathways to suppress anti-apoptosis, proliferation, chemoresistance, and EMT in SAS cells. Consistently, miR-200 upregulation has been demonstrated to inhibit cyclin D1, Bcl-2, and N-cadherin, as well as the transcription factors Snail, Slug, and ZEB1, in different cancer types [47,48].

In vivo antitumor efficacy and IVIS imaging studies involving SAS tumor-bearing mice

A SAS/luc tumor-bearing mouse model was established to determine the antitumor efficacy of different formulations *in vivo*. The combined treatment of pH-sensitive miR-200/omSLN-CMN + Iri/omLip-CMN displayed the most significant inhibitory effect on SAS-bearing mice, revealing the superior antitumor efficacy of this combined nanoparticle formulation among the various treatment groups (Figure 7A). Furthermore, the mice bearing the SAS tumor without treatment (CTR) displayed high bioluminescence intensity in the tumor region as shown by the IVIS images (Figure 7B). For comparison, the images were recorded with IVIS software, and the relative bioluminescence intensity is shown in the lower panel of Figure 7B. The bioluminescence intensity of the SAS tumor-bearing mice treated with various Iri and miR-200 formulations decreased, indicating the different tumor sizes (Figure 7B). Mice treated with miR-200/omSLN-CMN + Iri/omLip-CMN demonstrated the most substantial decrease in tumor size and luminescence intensity (Figures 7A–B). Interestingly, the antitumor efficacy of miR-200/omSLN-CMN + Iri/omLip-CMN was superior even to that of miR-200/omSLN-CMN + Onivyde. This finding was consistent with the TUNEL assay results (Figure 7C), which indicated that tumor-cell apoptosis and necrosis (green) were greatly intensified in the miR-200/omSLN-CMN + Iri/omLip-CMN group compared with those in the other groups. By contrast, *in vivo* TUNEL assay results (Figures S6A–B) verified that the apoptosis and necrosis of vessel cells (green) were most remarkably reduced in the miR-200/omSLN-CMN + Iri/omLip-CMN group. This finding suggested that miR-200/omSLN-CMN + Iri/omLip-CMN co-treatment had the lowest toxicity to vessel cells among all treatment groups. Notably, its toxicity was lower than that of Onivyde or miR-200/omSLN-CMN + Onivyde (Figure S6).

The evaluation of various formulations on body weight indicated that SAS-bearing mice treated with Iri showed a constant decrease in body weight (Figure 7D). All other groups exhibited mild escalations in body weight with slight individual differences (Figure 7D). Nevertheless, the curve of survival percentage demonstrated that Iri without nanoformulation caused 20% death of tumor-bearing mice (Figure S7) possibly because of the Iri-associated toxicity and the continuous body-weight loss during the 20 days. All

treatment groups with nanocarriers maintained 100% survival throughout the 20-day period (Figure S7), suggesting the safe compatibility of these delivery systems with the clinically available Onivyde.

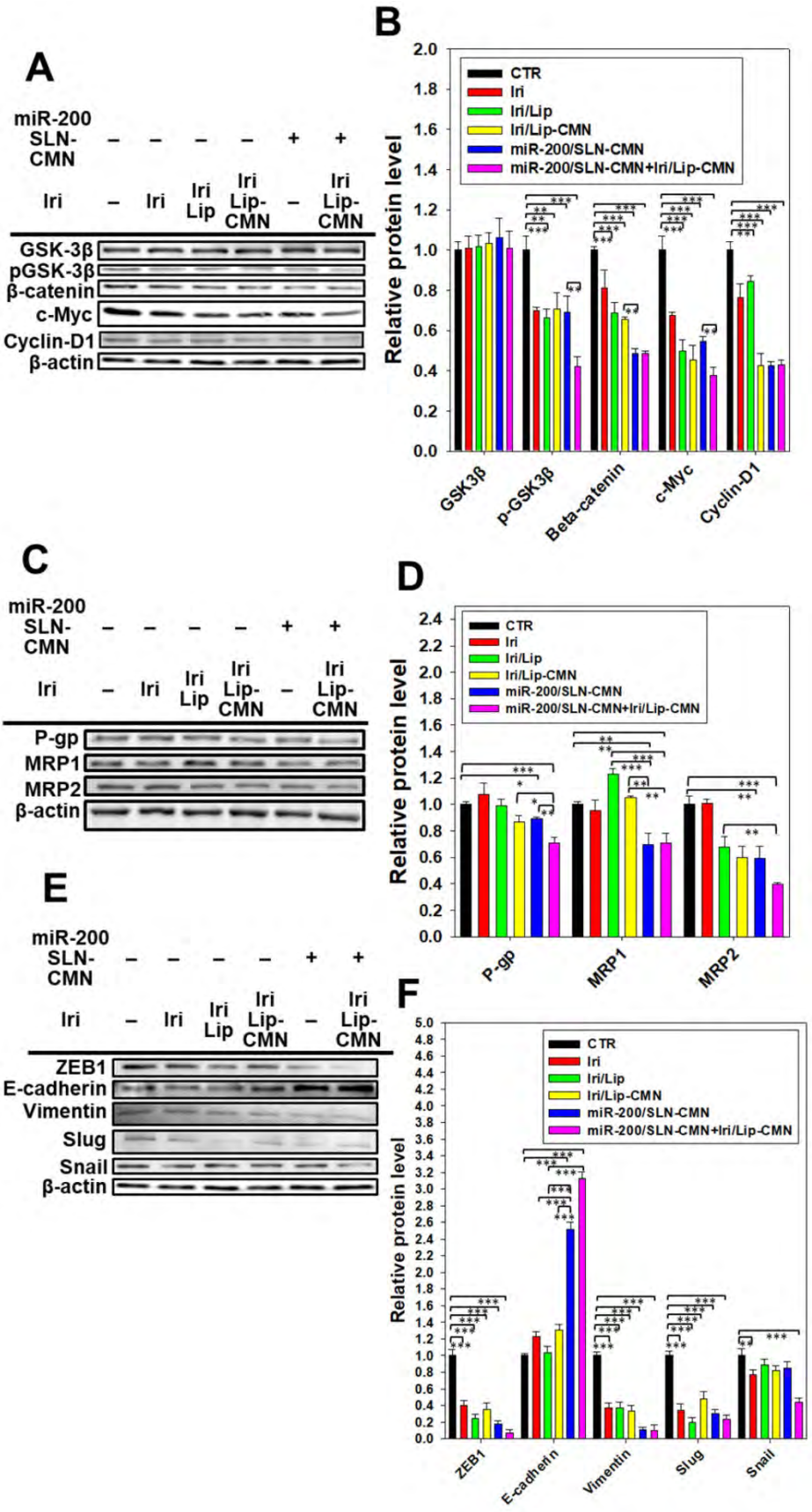

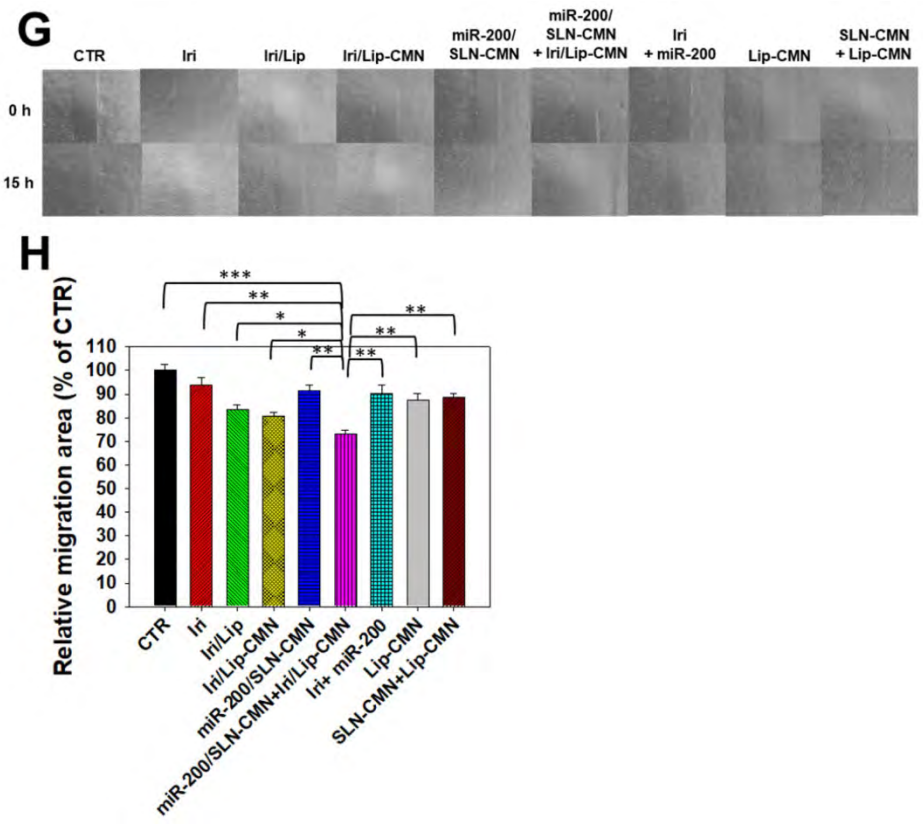

Figure 6. Effects of different formulations on diverse signaling pathways and relative migration percentage in SAS cells. SAS cells were pretreated with miR-200/SLN-CMN (100 nM) for 24 h and then with Iri or Iri/Lip-CMN (SAS = 0.7 μM) for 48 h. The protein expression levels of (A–B) Wnt/β-catenin, (C–D) MDR, and (E–F) EMT pathways were determined by Western blotting. (G) Cells were pretreated with different formulations for 15 h before the images were taken. (H) Quantification of the relative percentage of cell-migration area (*statistical significance at $P < 0.05$; **$P < 0.01$; ***$P < 0.001$).

In vivo biosafety evaluation: biochemical tests and H&E staining

Biochemical tests and H&E staining were conducted to detect organ functions and the histopathological characteristics of the various formulations used (Figures 8A–D). Serum GPT, CRE, and CK-MB, which are important biomarkers of the liver, kidney, and heart functions, respectively, were examined 1 day after the final treatment. Results showed that their levels considerably increased after the Iri treatments (Figures 8A–C), indicating the substantial damage inflicted by Iri to the liver, kidney, and heart. This finding may also partially explain the 20% death in the Iri-treated group of tumor-bearing mice (Figures S7). However, the serum levels of GPT, CRE, and CK-MB increased less after treatment with Iri in various liposomal formulations compared with the Iri group. In particular, these three biochemical markers maintained levels similar to those of the CTR groups ($P > 0.05$) after co-treatment with miR-200/omSLN-CMN + Iri/omLip-CMN (Figures 8A–C). The combined treatment of miR-200/omSLN-CMN and Iri/omLip-CMN displayed the lowest toxicity to the liver, kidney, and heart among all treatment groups, and the degree of toxicity was even lower than that of Onivyde alone or Onivyde + miR-200/omSLN-CMN (Figures 8A–C). This result was partially due to the design of the pH-sensitive omPEG layer in omSLN-CMN and omLip-CMN to prolong circulation time, promote pH-sensitive tumor accumulation, and induce the exposure of targeting peptides for the improved uptake and release of miR-200 and Iri into intracellular target sites of the cytoplasm and nucleus. These beneficial effects rendered the combined treatment more effective than Onivyde and reduced the Iri-inflicted damages to vital organs or tissues.

Additionally, results of *in vivo* HE staining of tumor tissues indicated that the CTR group had more tumor cells and larger nuclei than the other treatment groups (Figure 8D; panel 1). However, the tumor tissues of the miR-200/omSLN-CMN + Iri/omLip-CMN group showed the most obvious phenomenon of pyknosis, i.e., nuclear chromatin condensation (red circles; Figure 8D), which indicated tumor apoptosis and necrosis (Figure 8D; panel 1). The potential toxicity of these Iri and/or miR-200 formulations on the kidney, liver, and intestines was further examined through H&E staining (Figure 8D; panels 2–4). For comparison, the H&E staining of the kidney, liver, and intestines of the CTR groups exhibited integral

cell morphology (Figure 8D, panels 2–4). The intestinal, renal, and liver tissues of all treatment groups demonstrated interstitial hemorrhage (arrows), representing different degrees of tissue inflammation. The intestinal tissues also showed cell swelling, numerous vacuoles (potential indication of fatty degeneration; blue circles), and disordered cell arrangement, suggesting possible intestinal injury and inflammation (Figure 8D, panel 4). Interestingly, our *in vivo* results also indicated that miR-200/omSLN-CMN + Iri/omLip-CMN damaged the intestinal, renal, or liver cells to a lower extent and induced only minor histopathological abnormalities compared with the other treatment groups (Figure 8D, panels 2–4). Moreover, treatment with miR-200/omSLN-CMN + Iri/omLip-CMN confirmed a notable lessening of interstitial hemorrhage and tissue degeneration, which were most serious in the Iri group. Thus, tissue injury and inflammation were considerably more alleviated by the co-treatment of Iri/omLip-CMN and miR-200/omSLN-CMN than by Iri alone (Figure 8D, panels 2–4).

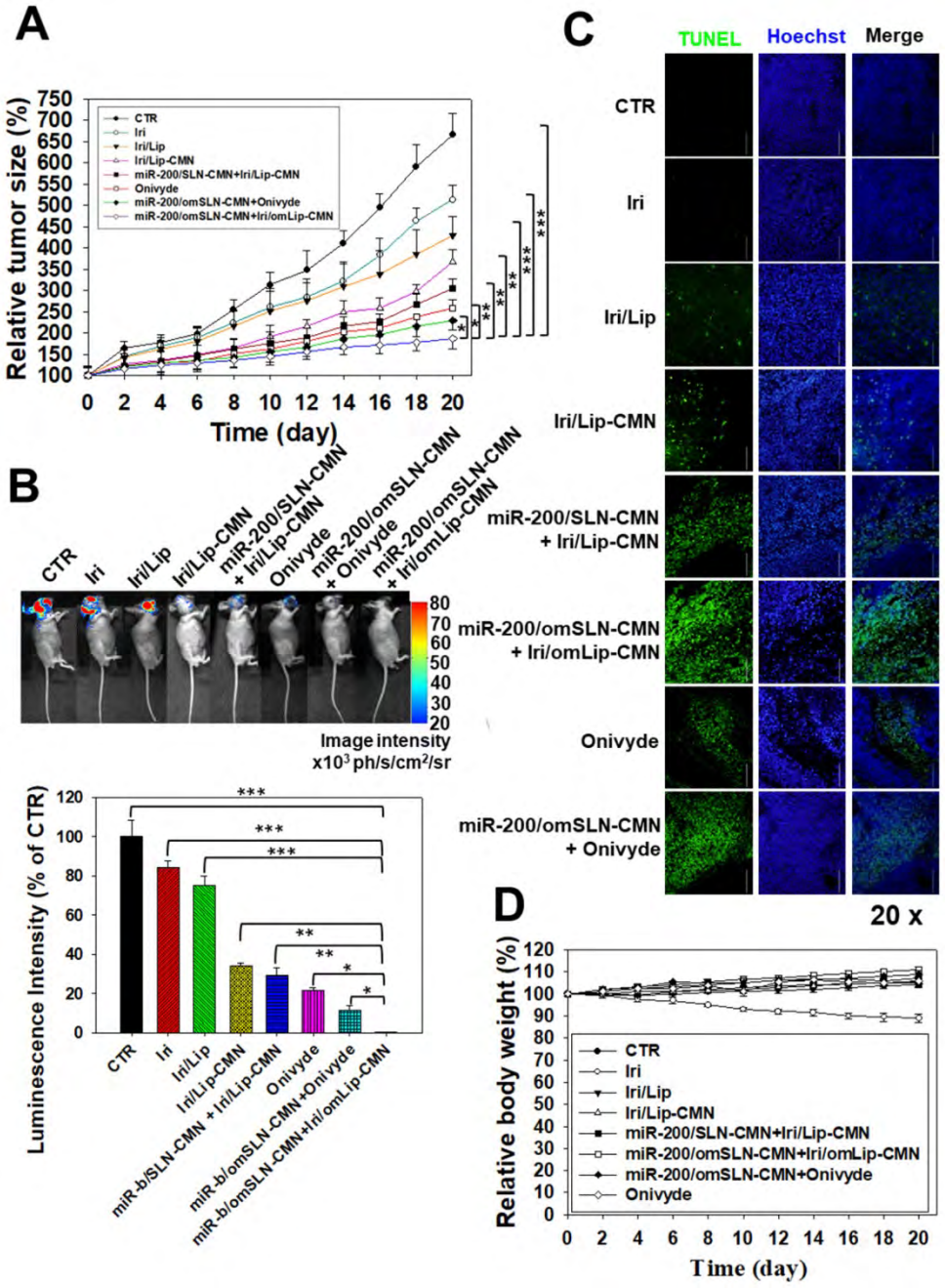

Figure 7. Antitumor efficacy of different formulations and relative body weight percentage on SAS/luc-bearing mice. (A) Antitumor efficacy of SAS/luc-bearing mice intravenously injected with different formulations. Tumor growth was measured with digital calipers every 2 days (*statistical significance at $P < 0.05$; **$P < 0.01$; ***$P < 0.001$). (B) IVIS images of SAS/*luc*-bearing mice treated with different formulations. (C) TUNEL analysis of *in vivo* apoptosis in SAS tumor cells (green) on the day after the last administration. Nuclei (blue) were stained with Hoechst. Scale bar, 100 μm. (D) Body weight of SAS/*luc*-bearing mice treated with different formulations for 20 days.

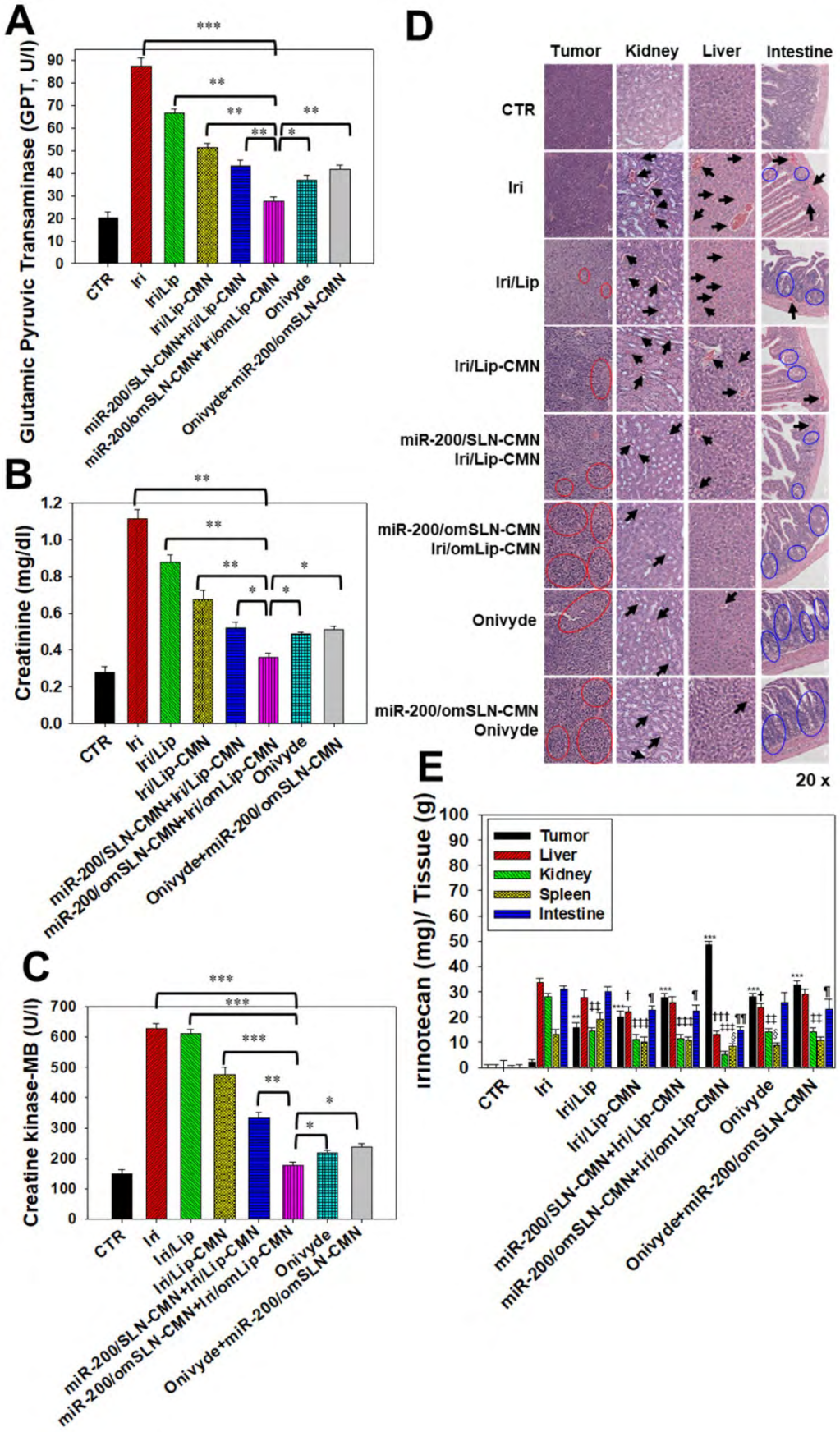
A
Glutamic Pyruvic Transaminase (GPT, U/l)
B
Creatinine (mg/dl)
C
Creatine kinase-MB (U/l)
CTR
Iri
Iri/Lip
Iri/Lip-CMN
miR-200/SLN-CMN+Iri/Lip-CMN
miR-200/omSLN-CMN+Iri/omLip-CMN
Onivyde
Onivyde+miR-200/omSLN-CMN
D
Tumor
Kidney
Liver
Intestine
CTR
Iri
Iri/Lip
Iri/Lip-CMN
miR-200/SLN-CMN
Iri/Lip-CMN
miR-200/omSLN-CMN
Iri/omLip-CMN
Onivyde
miR-200/omSLN-CMN
Onivyde
20 x
E
Irinotecan (mg)/ Tissue (g)
Tumor
Liver
Kidney
Spleen
Intestine
miR-200/SLN-CMN+Iri/Lip-CMN
miR-200/omSLN-CMN+Iri/omLip-CMN

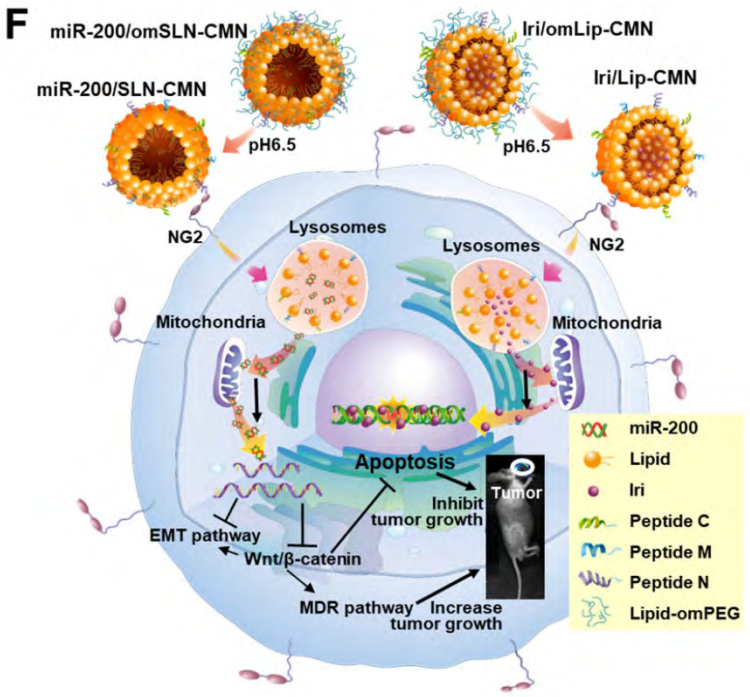

Figure 8. Biosafety and biodistribution studies on different formulations of SAS-bearing mice. (A–C) Blood biochemical indices of the (A) liver, (B) kidney, and (C) heart of mice treated with different formulations. *Statistical significance at $P < 0.05$; **$P < 0.01$; ***$P < 0.001$. (D) Histological photomicrographs of the tumor, kidney, liver, and intestinal sections stained with H&E. Red circles indicate necrosis or apoptosis; black arrows denote inflammation; blue circles correspond to cell injury. (E) Biodistribution study of different irinotecan formulations in SAS-bearing mice by using a UV spectrophotometer. *$P < 0.05$; **$P < 0.01$; ***$P < 0.001$ compared with Iri group for tumor. †$P < 0.05$; ††$P < 0.01$; †††$P < 0.001$ compared with Iri group for liver. ‡$P < 0.05$; ‡‡$P < 0.01$; ‡‡‡$P < 0.001$ compared with Iri group for kidney. §$P < 0.05$; §§$P < 0.01$; §§§$P < 0.001$ compared with Iri group for spleen. ¶$P < 0.05$; ¶¶$P < 0.01$; ¶¶¶$P < 0.001$ compared with Iri group for intestine. (F) Schematic of the molecular mechanisms by which miR-200/omSLN-CMN and Iri/omLip-CMN regulated multiple signaling pathways in the HNC model. NG2: nerve/glial antigen 2.

The biodistribution of Iri of different formulations in SAS-bearing mice was detected, and results demonstrated that Iri solution was distributed mainly in the liver, kidney, and intestines (Figure 8E). Nevertheless, miR-200/SLN-CMN + Iri/Lip-CMN, miR-200/omSLN-CMN + Iri/omLip-CMN, and Onivyde were primarily distributed in tumor tissues, particularly miR-200/SLN-CMN + Iri/Lip-CMN decorated with the pH-sensitive om-PEG (Figure 8E).

Considering the unmet medical need for HNC treatment, effective therapies should be based on the genetic or pathological characteristics or patient treatment history of various HNC types. SAS is a poorly differentiated, tumor-progression model of OSCC with aggressive invasion and migration [4, 49]. Thus, the encouraging preclinical findings in the current study suggested that the excellent tumor-accumulating feature of miR-200/SLN-CMN + Iri/Lip-CMN with its tumor-detachable PEG–lipid derivative layer may specifically deliver miR-200 and Iri into HNC tumor sites to modulate multiple signaling pathways and efficiently suppress tumor migration, resistance, and metastasis. Future work must focus on overcoming challenges such as scaling up/manufacturing and multifarious clinical trial requirements to enable the extensive clinical use of these two nanoparticle formulations. The schematic of the molecular mechanisms by which miR-200/omSLN-CMN and Iri/omLip-CMN regulated multiple signaling pathways in the HNC model is shown in Figure 8F.

Conclusion

A novel combination therapy was developed on the basis of the delivery of miR-200 and Iri by the corresponding carrier systems for the potential treatment of HNC. The functions of these nanoparticles were as follows: (1) decreasing noncancerous cellular uptake through the protection provided by the outer cleavable PEG–lipid shell, (2) enhancing passive tumor targeting via the EPR effect, and (3) improving active tumor targeting via specific ligand–receptor binding. The apoptosis of HNC cells treated with the combinatorial therapy was significantly induced by regulating various pathways, such as the Wnt/β-catenin, MDR, and EMT pathways. The therapeutic efficacy and safety of co-treatment with pH-sensitive and peptide-conjugated nanoparticles were better than those of the commercially available Onivyde and other formulations in tumor-bearing HNC mice. Overall, this study suggested that chemo- and gene therapy co-treatment with pH-sensitive and targeting peptide-

modified nanoparticles may be an innovative strategy for HNC treatment.

Abbreviations

HNC: head and neck cancer; SAS: human tongue squamous carcinoma cell line; miR: microRNA; Iri: irinotecan; Topo: topoisomerase; MDR: multidrug resistance; P-gp: P-glycoprotein; MRP: MDR-associated proteins; EMT: epithelial–mesenchymal transition; ZEB1: zinc finger E-box binding homeobox 1; SLN: solid lipid nanoparticles; Lip: liposomes; CPP: cell-penetrating peptide; NG2: nerve/glial antigen 2; N peptide: a NG2-binding peptide; M peptide: one mitochondrion-directed apoptosis-inducing peptide; C peptide: one cell-penetrating peptide with high potency and selectivity against cancer cells; omPEG: O′-methyl polyethylene glycol; omSLN-CMN and omLip-CMN: SLN and Lip modified with pH-sensitive PEG-lipid derivative (lipid-imine-omPEG) and peptide C, M, and N; EPR: enhanced permeability and retention; MALDI-TOF MS: matrix-assisted laser desorption ionization time-of-flight mass spectrometry; TEM: transmission electron microscopy; EE%: encapsulation efficiency; DL%: drug-loading capacity; PDI: polydispersity index; NOK: normal oral keratinocyte; FBS: fetal bovine serum; DMA: 5-(N,N-dimethyl) amiloride; CPZ: chlorpromazine; CLSM: confocal laser scanning microscopy; SRB: sulforhodamine B; PI: propidium iodide; SDS-PAGE: sodium dodecyl sulfate–polyacrylamide gel; CTR: control; H&E: hematoxylin and eosin; GPT: glutamate pyruvate transaminase; CRE: creatinine; CK-MB: creatine kinase-MB; DNR: daunorubicin; LysoGreen: LysoTracker® Green; TUNEL: terminal deoxynucleotidyl transferase dUTP nick end labeling; ABC: ATP-binding cassette.

Supplementary Material

Supplementary figures and tables.
http://www.thno.org/v10p6695s1.pdf

Acknowledgments

This project was financially supported by grants from the Ministry of Science and Technology (MOST) of Taiwan (MOST 106-2320-B-010-005 and MOST 107-2320-B-010-015-MY3), the Veterans General Hospitals and University System of Taiwan Joint Research Program (VGHUST108-G2-1-2 and VGHUST109-V7-3-2), the National Yang-Ming University and Cheng Hsin General Hospital (CY10839 and CY10935), the Center for Advanced Pharmaceutics and Drug Delivery Research, Yin Yen-Liang Foundation Development and Construction Plan of the School of Medicine, National Yang-Ming University, Ministry of Education of Taiwan (Aiming for the Top University Plan). We also thank the Taiwan Animal Consortium (MOST 107-2319-B-001-002)-Taiwan Mouse Clinic for technical support in animal imaging experiment.

Competing Interests

The authors have declared that no competing interest exists.

References

1. Hsu DS, Hwang WL, Yuh CH, Chu CH, Ho YH, Chen PB, et al. Lymphotoxin-beta Interacts with Methylated EGFR to Mediate Acquired Resistance to Cetuximab in Head and Neck Cancer. Clin Cancer Res. 2017; 23: 4388-401.
2. Abdulla R, Adyanthaya S, Kini P, Mohanty V, D'Souza N, Subbannayya Y. Clinicopathological analysis of oral squamous cell carcinoma among the younger age group in coastal Karnataka, India: A retrospective study. J Oral Maxillofac Pathol. 2018; 22: 180-7.
3. Shindoh M, Higashino F, Kaya M, Yasuda M, Funaoka K, Hanzawa M, et al. Correlated expression of matrix metalloproteinases and ets family transcription factor E1A-F in invasive oral squamous-cell-carcinoma-derived cell lines. Am J Pathol. 1996; 148: 693-700.
4. Suzuki S, Toyoma S, Tsuji T, Kawasaki Y, Yamada T. CD147 mediates transforming growth factor-β1-induced epithelial-mesenchymal transition and cell invasion in squamous cell carcinoma of the tongue. Exp Ther Med. 2019; 17: 2855-60.
5. Pai S, Bamodu OA, Lin YK, Lin CS, Chu PY, Chien MH, et al. CD47-SIRPα Signaling Induces Epithelial-Mesenchymal Transition and Cancer Stemness and Links to a Poor Prognosis in Patients with Oral Squamous Cell Carcinoma. Cells. 2019; 8.
6. Ku GY. Systemic therapy for esophageal cancer: chemotherapy. Chin Clin Oncol. 2017; 6: 49.
7. Hirano H, Kato K. Systemic treatment of advanced esophageal squamous cell carcinoma: chemotherapy, molecular-targeting therapy and immunotherapy. Jpn J Clin Oncol. 2019; 49: 412-20.
8. Krbal L, Hanusova V, Soukup J, John S, Matouskova P, Ryska A. Contribution of in vitro comparison of colorectal carcinoma cells from primary and metastatic lesions to elucidation of mechanisms of tumor progression and response to anticancer therapy. Tumour Biol. 2016; 37: 9565-78.
9. Xu Y, Villalona-Calero MA. Irinotecan: mechanisms of tumor resistance and novel strategies for modulating its activity. Ann Oncol. 2002; 13: 1841-51.
10. Gottesman MM, Fojo T, Bates SE. Multidrug resistance in cancer: role of ATP-dependent transporters. Nat Rev Cancer. 2002; 2: 48-58.
11. Yang Y, Wang G, Zhu D, Huang Y, Luo Y, Su P, et al. Epithelial-mesenchymal transition and cancer stem cell-like phenotype induced by Twist1 contribute to acquired resistance to irinotecan in colon cancer. Int J Oncol. 2017; 51: 515-24.
12. Abdel-Rahman WM, Al-Khayyal NA, Nair VA, Aravind SR, Saber-Ayad M. Role of AXL in invasion and drug resistance of colon and breast cancer cells and its association with p53 alterations. World J Gastroenterol. 2017; 23: 3440-8.
13. Sinicrope FA, Okamoto K, Kasi PM, Kawakami H. Molecular Biomarkers in the Personalized Treatment of Colorectal Cancer. Clin Gastroenterol Hepatol. 2016; 14: 651-8.
14. Shi C, Huang F, Gu X, Zhang M, Wen J, Wang X, et al. Adipogenic miRNA and meta-signature miRNAs involved in human adipocyte differentiation and obesity. Oncotarget. 2016; 7: 40830-45.
15. Tanaka F, Yoshimoto S, Okamura K, Ikebe T, Hashimoto S. Nuclear PKM2 promotes the progression of oral squamous cell carcinoma by inducing EMT and post-translationally repressing TGIF2. Oncotarget. 2018; 9: 33745-61.
16. Prokopi M, Kousparou CA, Epenetos AA. The Secret Role of microRNAs in Cancer Stem Cell Development and Potential Therapy: A Notch-Pathway Approach. Front Oncol. 2014; 4: 389.
17. Brabletz S, Bajdak K, Meidhof S, Burk U, Niedermann G, Firat E, et al. The ZEB1/miR-200 feedback loop controls Notch signalling in cancer cells. EMBO J. 2011; 30: 770-82.
18. Kim EJ, Kim JS, Lee S, Lee H, Yoon JS, Hong JH, et al. QKI, a miR-200 target gene, suppresses epithelial-to-mesenchymal transition and tumor growth. Int J Cancer. 2019; 145: 1585-95.
19. Peng DH, Kundu ST, Fradette JJ, Diao L, Tong P, Byers LA, et al. ZEB1 suppression sensitizes KRAS mutant cancers to MEK inhibition by an IL17RD-dependent mechanism. Sci Transl Med. 2019; 11.
20. Kim DY, Lee SS, Bae YK. Colorectal cancer cells differentially impact migration and microRNA expression in endothelial cells. Oncol Lett. 2019; 18: 6361-70.
21. Chen X, Zhu Q, Xu X, Shen S, Zhang Y, Mo R. Sequentially Site-Specific Delivery of Apoptotic Protein and Tumor-Suppressor Gene for Combination Cancer Therapy. Small. 2019: e1902998.
22. Juang V, Chang CH, Wang CS, Wang HE, Lo YL. pH-Responsive PEG-Shedding and Targeting Peptide-Modified Nanoparticles for

Dual-Delivery of Irinotecan and microRNA to Enhance Tumor-Specific Therapy. Small. 2019; 15: e1903296.
23. Jones SW, Christison R, Bundell K, Voyce CJ, Brockbank SM, Newham P, et al. Characterisation of cell-penetrating peptide-mediated peptide delivery. Br J Pharmacol. 2005; 145: 1093-102.
24. Brand C, Schliemann C, Ring J, Kessler T, Baumer S, Angenendt L, et al. NG2 proteoglycan as a pericyte target for anticancer therapy by tumor vessel infarction with retargeted tissue factor. Oncotarget. 2016; 7: 6774-89.
25. Guan YY, Luan X, Xu JR, Liu YR, Lu Q, Wang C, et al. Selective eradication of tumor vascular pericytes by peptide-conjugated nanoparticles for antiangiogenic therapy of melanoma lung metastasis. Biomaterials. 2014; 35: 3060-70.
26. Park H, Tsutsumi H, Mihara H. Cell-selective intracellular drug delivery using doxorubicin and alpha-helical peptides conjugated to gold nanoparticles. Biomaterials. 2014; 35: 3480-7.
27. Lin KH, Hong ST, Wang HT, Lo YL, Lin AM, Yang JC. Enhancing Anticancer Effect of Gefitinib across the Blood-Brain Barrier Model Using Liposomes Modified with One alpha-Helical Cell-Penetrating Peptide or Glutathione and Tween 80. Int J Mol Sci. 2016; 17: E1998.
28. Xie R, Lian S, Peng H, OuYang C, Li S, Lu Y, et al. Mitochondria and Nuclei Dual-Targeted Hollow Carbon Nanospheres for Cancer Chemophotodynamic Synergistic Therapy. Mol Pharm. 2019; 16: 2235-48.
29. Zhang J, Chen L, Shen B, Chen L, Mo J, Feng J. Dual-Sensitive Graphene Oxide Loaded with Proapoptotic Peptides and Anticancer Drugs for Cancer Synergetic Therapy. Langmuir. 2019; 35: 6120-8.
30. Yan J, Chen J, Zhang N, Yang Y, Zhu W, Li L, et al. Mitochondria-targeted tetrahedral DNA nanostructures for doxorubicin delivery and enhancement of apoptosis. J Mater Chem B. 2020; 8: 492-503.
31. Bang YJ, Ruiz EY, Van Cutsem E, Lee KW, Wyrwicz L, Schenker M, et al. Phase III, randomised trial of avelumab versus physician's choice of chemotherapy as third-line treatment of patients with advanced gastric or gastro-oesophageal junction cancer: primary analysis of JAVELIN Gastric 300. Ann Oncol. 2018; 29: 2052-60.
32. Li H, Zhao Y, Jia Y, Qu C, Li J. Covalently assembled dopamine nanoparticle as an intrinsic photosensitizer and pH-responsive nanocarrier for potential application in anticancer therapy. Chem Commun (Camb). 2019; 55: 15057-60.
33. Fan F, Yu Y, Zhong F, Gao M, Sun T, Liu J, et al. Design of Tumor Acidity-Responsive Sheddable Nanoparticles for Fluorescence/Magnetic Resonance Imaging-Guided Photodynamic Therapy. Theranostics. 2017; 7: 1290-302.
34. Chen Y, Gao D-Y, Huang L. In vivo delivery of miRNAs for cancer therapy: challenges and strategies. Adv Drug Deliv Rev. 2015; 81: 128-41.
35. Behzadi S, Serpooshan V, Tao W, Hamaly MA, Alkawareek MY, Dreaden EC, et al. Cellular uptake of nanoparticles: journey inside the cell. Chem Soc Rev. 2017; 46: 4218-44.
36. Sahay G, Alakhova DY, Kabanov AV. Endocytosis of nanomedicines. J Control Release. 2010; 145: 182-95.
37. Ma D. Enhancing endosomal escape for nanoparticle mediated siRNA delivery. Nanoscale. 2014; 6: 6415-25.
38. Goyal Y, Koul A, Ranawat P. Ellagic acid ameliorates cisplatin induced hepatotoxicity in colon carcinogenesis. Environ Toxicol. 2019; 34: 804-13.
39. Xin L-T, Liu L, Shao C-L, Yu R-L, Chen F-L, Yue S-J, et al. Discovery of DNA Topoisomerase I Inhibitors with Low-Cytotoxicity Based on Virtual Screening from Natural Products. Mar Drugs. 2017; 15: 217.
40. Cheng X, Xu X, Chen D, Zhao F, Wang W. Therapeutic potential of targeting the Wnt/β-catenin signaling pathway in colorectal cancer. Biomed Pharmacother. 2019; 110: 473-81.
41. Woo MS, Choi HS, Seo MJ, Jeon HJ, Lee BY. Ellagic acid suppresses lipid accumulation by suppressing early adipogenic events and cell cycle arrest. Phytother Res. 2015; 29: 398-406.
42. Mohammad Khanlou E, Atashbar S, Kahrizi F, Shokouhi Sabet N, Salimi A. Bevacizumab as a monoclonal antibody inhibits mitochondrial complex II in isolated rat heart mitochondria: ameliorative effect of ellagic acid. Drug Chem Toxicol. 2020: 1-8.
43. Juang V, Lee HP, Lin AM, Lo YL. Cationic PEGylated liposomes incorporating an antimicrobial peptide tilapia hepcidin 2-3: an adjuvant of epirubicin to overcome multidrug resistance in cervical cancer cells. Int J Nanomedicine. 2016; 11: 6047-64.
44. Lin GL, Ting HJ, Tseng TC, Juang V, Lo YL. Modulation of the mRNA-binding protein HuR as a novel reversal mechanism of epirubicin-triggered multidrug resistance in colorectal cancer cells. PLoS One. 2017; 12: e0185625.
45. Ghahhari NM, Babashah S. Interplay between microRNAs and WNT/beta-catenin signalling pathway regulates epithelial-mesenchymal transition in cancer. Eur J Cancer. 2015; 51: 1638-49.
46. Goyal Y, Koul A, Ranawat P. Ellagic acid ameliorates cisplatin toxicity in chemically induced colon carcinogenesis. Mol Cell Biochem. 2019; 453: 205-15.
47. Fu J, Shrivastava A, Shrivastava SK, Srivastava RK, Shankar S. Triacetyl resveratrol upregulates miRNA-200 and suppresses the Shh pathway in pancreatic cancer: A potential therapeutic agent. Int J Oncol. 2019; 54: 1306-16.
48. Kozak J, Jonak K, Maciejewski R. The function of miR-200 family in oxidative stress response evoked in cancer chemotherapy and radiotherapy. Biomed Pharmacother. 2020; 125: 110037.
49. Wei LY, Lee JJ, Yeh CY, Yang CJ, Kok SH, Ko JY, et al. Reciprocal activation of cancer-associated fibroblasts and oral squamous carcinoma cells through CXCL1. Oral Oncol. 2019; 88: 115-23.

NANO · MICRO small
www.small-journal.com

pH-Responsive PEG-Shedding and Targeting Peptide-Modified Nanoparticles for Dual-Delivery of Irinotecan and microRNA to Enhance Tumor-Specific Therapy

*Vivian Juang, Chih-Hsien Chang, Chen-Shen Wang, Hsin-Ell Wang, and Yu-Li Lo**

Irinotecan is one of the main chemotherapeutic agents for colorectal cancer (CRC). MicroRNA-200 (miR-200) has been reported to inhibit metastasis in cancer cells. Herein, pH-sensitive and peptide-modified liposomes and solid lipid nanoparticles (SLN) are designed for encapsulation of irinotecan and miR-200, respectively. These peptides include one cell-penetrating peptide, one ligand targeted to tumor neovasculature undergoing angiogenesis, and one mitochondria-targeting peptide. The peptide-modified nanoparticles are further coated with a pH-sensitive PEG-lipid derivative with an imine bond. These specially-designed nanoparticles exhibit pH-responsive release, internalization, and intracellular distribution in acidic pH of colon cancer HCT116 cells. These nanoparticles display low toxicity to blood and noncancerous intestinal cells. Delivery of miR-200 by SLN further increases the cytotoxicity of irinotecan-loaded liposomes against CRC cells by triggering apoptosis and suppressing RAS/β-catenin/ZEB/multiple drug resistance (MDR) pathways. Using CRC-bearing mice, the in vivo results further indicate that irinotecan and miR-200 in pH-responsive targeting nanoparticles exhibit positive therapeutic outcomes by inhibiting colorectal tumor growth and reducing systemic toxicity. Overall, successful delivery of miR and chemotherapy by multifunctional nanoparticles may modulate β-catenin/MDR/apoptosis/metastasis signaling pathways and induce programmed cancer cell death. Thus, these pH-responsive targeting nanoparticles may provide a potential regimen for effective treatment of colorectal cancer.

1. Introduction

Colorectal cancer (CRC) is one of the major causes of cancer-related morbidity worldwide.[1] Irinotecan (Iri), a water-soluble camptothecin, is one of the first-line therapeutic agents for advanced or metastatic colorectal cancer.[2] Irinotecan functions by avoiding religation of the DNA strand via forming a cleavable drug-DNA-topoisomerase I complex, thus causing lethal double-strand DNA breakage and cell death.[3] However, irinotecan is remarkably effluxed by P-glycoprotein (P-gp) and multidrug resistance (MDR)-associated proteins (MRPs) in tumor cells.[4] Resistance and adverse events, including diarrhea, nausea, and vomiting usually occur in later stages of irinotecan therapy.[5,6]

MicroRNAs (miRNAs; miRs) play critical roles in modulating mRNA translation.[7] Upregulation of hsa-miR-200c-3p may suppress epithelial-mesenchymal transition (EMT) and inhibit metastasis through suppression of ZEB1/2, Snail and Slug.[8,9] Furthermore, miR-200 downregulated ZEB1 and vimentin, and increased cancer cell sensitivity to gemcitabine.[10] Nevertheless, the use of miR-200 alone was not sufficient as a single anticancer agent. Additionally, there are obstacles for miR delivery into cells, including rapid degradation in the systemic circulation, fast detection by the immune system, low cellular uptake, and poor endosomal escape.[11] Hence, we designed solid lipid nanoparticles (SLN) and liposomes (Lip) to specifically and separately deliver hsa-miR-200c-3p and irinotecan. We prepared SLN and Lip using lipids modified with peptides that exert various functions. Cell-penetrating peptides (CPPs) may enhance the intracellular uptake and endosomal escape of drug delivery systems.[12] **H peptide**, isolated by phage display for binding to nerve/glial antigen 2 (NG2), acted as a ligand in the present study.[13] NG2, a transmembrane proteoglycan, is highly expressed in tumor neovasculature undergoing angiogenesis, but is not detectable in normal quiescent vasculature.[13–15] **RF peptide**, a potent CPP screened from a library of alpha-helix peptides, was found to show higher normal cell compatibility than TAT peptide.[16] Additionally, peptide RF also induced cell death in tumor cells.[16] **K peptide**, a mitochondria-targeting

V. Juang, C.-H. Chang, C.-S. Wang, Prof. Y.-L. Lo
Department and Institute of Pharmacology
National Yang-Ming University
Taipei 112, Taiwan
E-mail: yulilo@ym.edu.tw
Prof. H.-E. Wang
Department of Biomedical Imaging and Radiological Sciences
National Yang-Ming University
Taipei 112, Taiwan
Prof. Y.-L. Lo
Faculty of Pharmacy
National Yang-Ming University
Taipei 112, Taiwan
Prof. Y.-L. Lo
Center for Advanced Pharmaceutics and Drug Delivery Research
National Yang-Ming University
Taipei 112, Taiwan
The ORCID identification number(s) for the author(s) of this article can be found under https://doi.org/10.1002/smll.201903296.

DOI: 10.1002/smll.201903296

peptide, displays characteristic KLA residues, which can increase nanoparticle uptake into cancer cells, especially to mitochondria.[17,18] Moreover, nanoparticles coated with K peptide might reduce mitochondrial membrane potential, produce ATP depletion, trigger tumor cell apoptosis, and consequently circumvent MDR in cancer chemotherapy.[17,19]

In addition, to avoid degradation of these targeting or cell-penetrating peptides in systemic circulation, we constructed these peptide-modified SLN and Lip with an intelligent pH-sensitive cleavable PEG-shedding system that could utilize the low extracellular pH of 6.5 in the tumor microenvironment. This long-chain PEG 5000 polymer, O'-methyl polyethylene glycol (**omPEG**), was designed to conjugate with lipid to form a pH-responsive imine bond. This specific pH-sensitive PEG-lipid derivative (lipid-imine-omPEG) was used to prepare the SLN and Lip, namely, **omSLN** and **omLip** with different peptide modification to form **omSLN-RFKH** and **omLip-RFKH** (**Figure 1**A). The increased tumor accumulation of these nanoparticles is at least partially due to the enhanced permeability and retention (EPR) effect. Furthermore, the acidic extracellular pH of tumors serves as an intrinsic stimulus for provoking the exposure of multifunctional SLN and Lip modified with CPP RF, ligand H, and the mitochondria-targeting peptide K (**SLN-RFKH** and **Lip-RFKH**). The rationale for the combinatorial therapy of miR-200 and irinotecan is to provide the advantages of increasing the anticancer efficacy while reducing the side effects of irinotecan via multiple signaling modulation in tumor metastasis and chemoresistance by miR-200 (Figure 1A).

2. Results

2.1. Synthesis of DSPE-omPEG and DSPE-PEG-Peptide

1,2-Distearoyl-sn-glycero-3-phosphoethanolamine-polyethylene glycol-2000-peptide (DSPE-PEG-peptide) was synthesized by conjugating DSPE-PEG-maleimide to the cysteine residue of peptide RF, K, and H to form a thioether bond. The mass of DSPE-PEG-peptide was confirmed by mass spectrometry (Figure S1A, Supporting Information), suggesting that the indicated peptides were conjugated to DSPE-PEG (Figure 1B–D). Moreover, according to ^{1}H NMR analyses, the spectrum of DSPE-imine-omPEG displayed an extra peak at 9.33. ppm (Figure 1E; Figure S1D, Supporting Information) compared with the spectra of omPEG (Figure S1B, Supporting Information) and DSPE (Figure S1C, Supporting Information), indicating that the pH-sensitive imine bond was formed between DSPE and omPEG.

2.2. Characterization of Multifunctional Lip and SLN

Iri/omLip-RFKH and miR-200/omSLN-RFKH displayed a homogeneous and narrow size distribution (**Table 1**). The liposomes were negatively charged and the SLN were positively charged (Table 1). Encapsulation efficiency % of Iri- or miR-loaded Lip or SLN were all above 88% and the corresponding drug loading capacity % were higher than 14% (Table 1; **Figure 2**A). We found that the particle size and zeta potential of these nanoparticles remained constant with a narrow size distribution (PDI ≈ 0.1) after storage at 4 °C for 28 d (Figure 2B,C; Figure S2A,B, Supporting Information). Furthermore, naked miR was degraded or aggregated after incubation with 1% RNase or 50% fetal bovine serum (FBS) for 24 h, as shown by running agarose gel electrophoresis (Figure 2D; Lanes 6 and 10). Remarkably, the miR samples were well protected by omSLN-RFKH from degradation or aggregation by RNase or FBS (Figure 2D; Lanes 9 and 13). Interestingly, SLN-RFKH without pH-sensitive layer might also provide the similar protection under the attack of 50% FBS (Figure 2D; Lane 12). However, SLN without pH-sensitive layer and peptide-modification did not prevent miR from degradation or aggregation by the attack of 50% FBS (Figure 2D; Lane 11), even though SLN with or without modification protected the miR degradation induced by 1% RNase (Figure 2D; Lanes 7–9). Additionally, the liposomes showed spherical particles and no large aggregates were found, as demonstrated by transmission electron microscope (TEM) (Figure 2E) and cryo-TEM (Figure 2F). The outer layer exhibited the typical bilayer structure of liposomes and crystals of irinotecan were observed in the core, as shown in the cryo-TEM images (Figure 2F).

2.3. Characterization of pH-Responsive Lip or SLN

For pH-sensitive release of irinotecan or miR at both pH 7.4 and 6.5 at 37 °C, more than 95% of irinotecan or miR was released from irinotecan or miR solution (as control) during the first 1 h, and the release reached 100% within 24 h (**Figure 3**A; Figure S2C, Supporting Information). However, the percentage of irinotecan released from omLip-RFKH up to 24 h was 46.86 ± 2.34% at pH 7.4, which was increased to 67.89 ± 1.88% at pH 6.5 (Figure 3A). Thus, omLip exhibited a sustained irinotecan release profile at pH 7.4 and a significant increase under mimic acidic tumor pH. Additionally, nanoparticles prepared with DSPE-PEG5000 without the formation of imine bond (Iri/PEG-Lip-RFKH) were also used for comparison. The release trend of irinotecan from Iri/PEG Lip-RFKH at both pH 6.5 and 7.4 were similar to that of omLip-RFKH at pH 7.4, suggesting no pH-dependent release for Iri/PEG Lip-RFKH (Figure 3A). Importantly, the release profile of miR from omSLN-RFKH at pH 6.5 and 7.4 also displayed the similar pH-responsive trend as that of Iri/omLip-RFKH (Figure S2C, Supporting Information), indicating the pH-sensitive deshielding of omLip or omSLN formulation at pH 6.5 to expose the inner Lip-RFKH or SLN-RFKH for release of irinotecan or miR (Figure 3A; Figure S2C, Supporting Information).

Furthermore, DNR (a probe for irinotecan) in omLip-RFKH showed a much higher cellular uptake after incubation in phosphate buffered saline (PBS) at pH 6.5 than at pH 7.4 (Figure 3B). The addition of miR-200/omSLN-RF+K+H further enhanced the intracellular accumulation of DNR from omLip-RFKH at pH 6.5. Interestingly, without the impedance of omPEG long-chain, the combined treatment of Iri/Lip-RF+K+H and miR-200/SLN-RF+K+H displayed the high cellular uptake into human colorectal cancer HCT116 cells at pH 6.5 and pH 7.4 (no imine bond; Figure 3B). However, there was no pH-responsive cellular uptake of DNR from PEG-Lip-RFKH

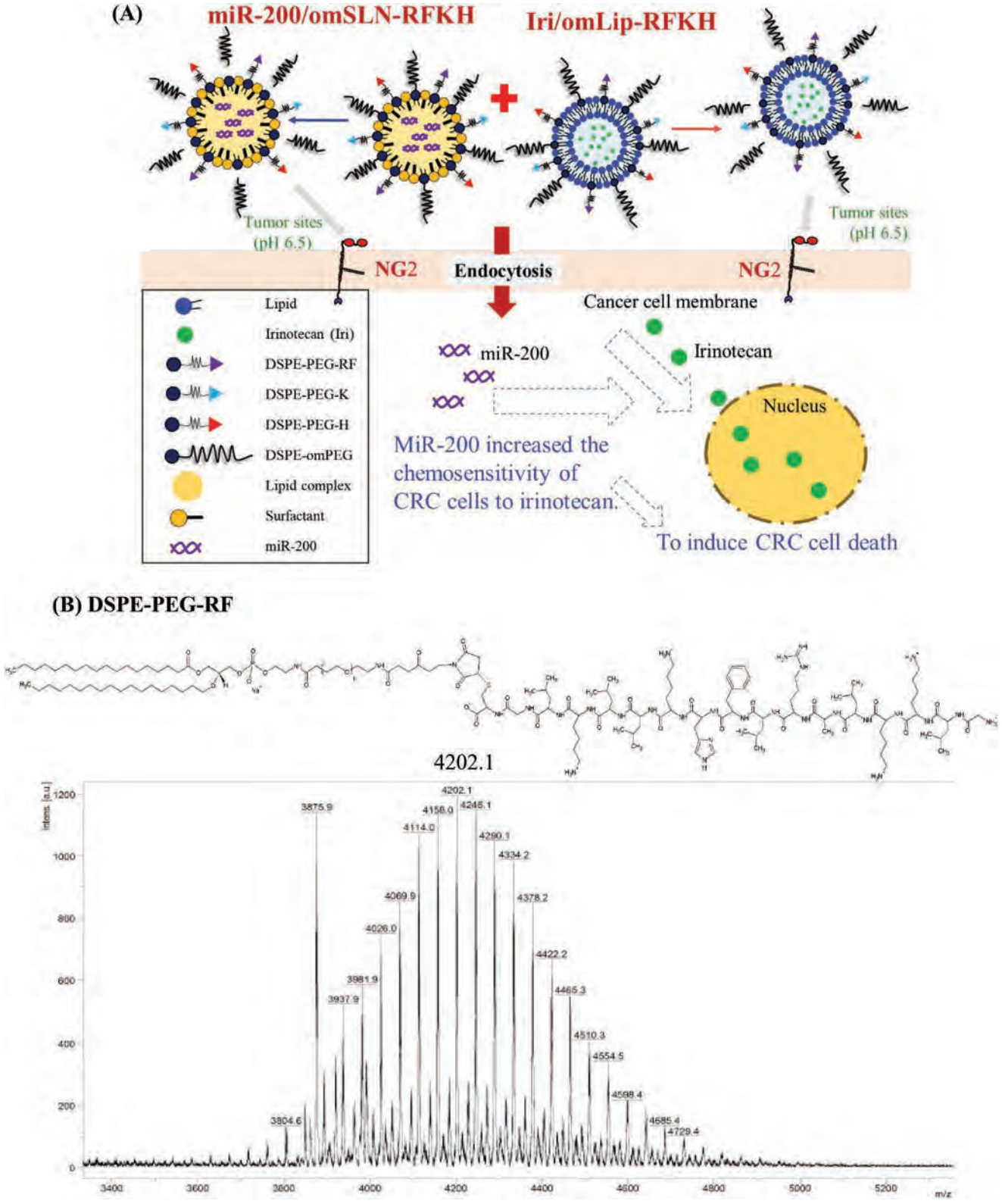

Figure 1. A) A schematic diagram for the design of pH-sensitive and peptide-modified PEGylated liposomes (Lip) and solid lipid nanoparticles (SLN) incorporating irinotecan (Iri) and miR-200, respectively. B–D) Conjugation of DSPE-PEG-maleimide to RF, K, and H. The structure and mass spectra of the corresponding peptide-conjugates of B) DSPE-PEG-RF, C) DSPE-PEG-K and D) DSPE-PEG-H as detected by MALDI-TOF mass spectrometer. E) ^{1}H NMR of DSPE-imine-omPEG conjugate.

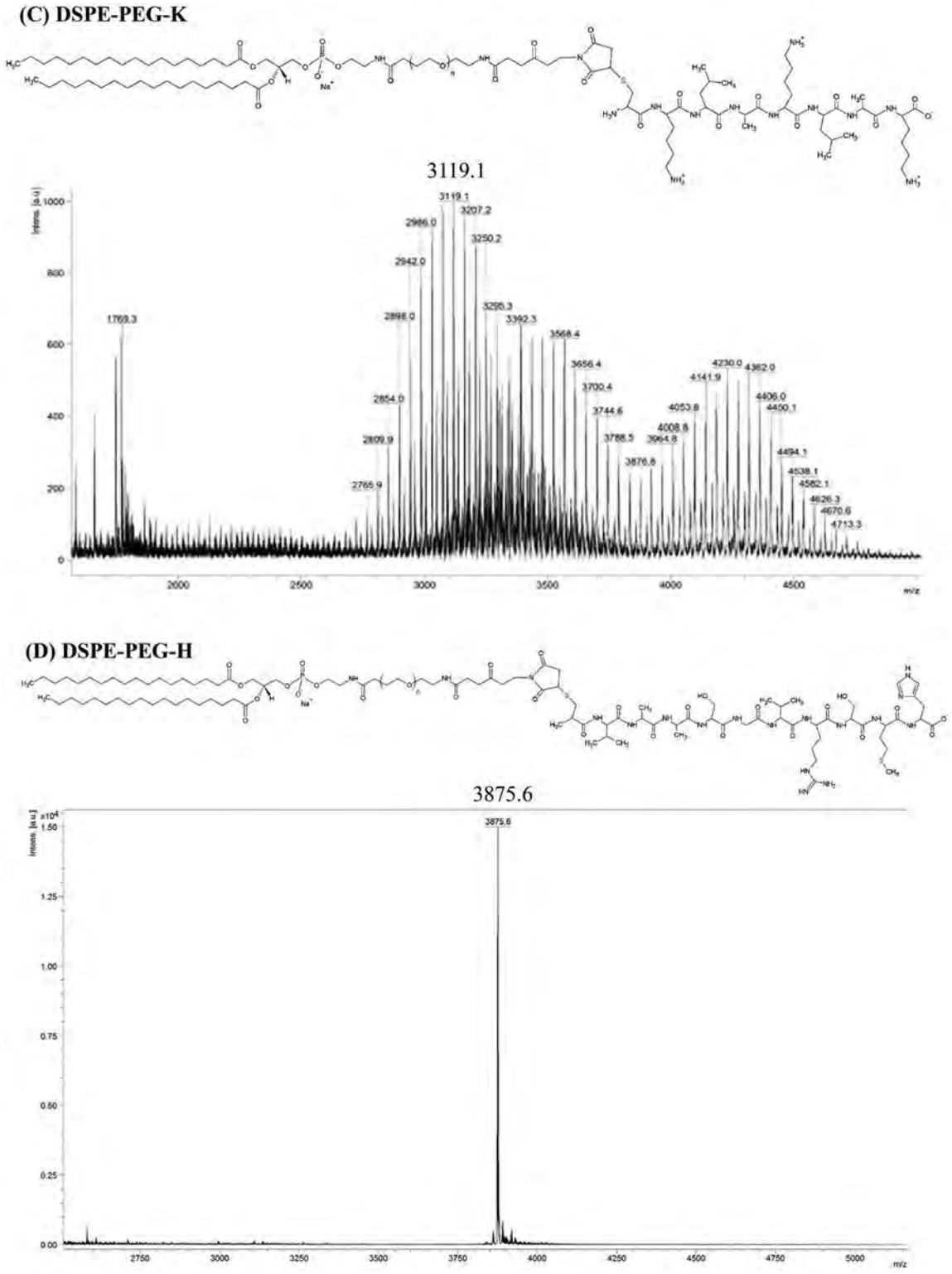

Figure 1. Continued.

(no imine bond; Figure 3B). Moreover, the confocal laser scanning microscope (CLSM) results shown in Figure 3C revealed that after 24 h of incubation, DNR from the pH-responsive omLip-RFKH was predominantly localized in the nucleus of HCT116 cells at pH 6.5, which confirmed the final destination of the topoisomerase inhibitor carried by omLip-RFKH into the nucleus to induce cytotoxicity (Figure 3C). We further verified that DNR in Lip-RFKH was escaped from endosomes and

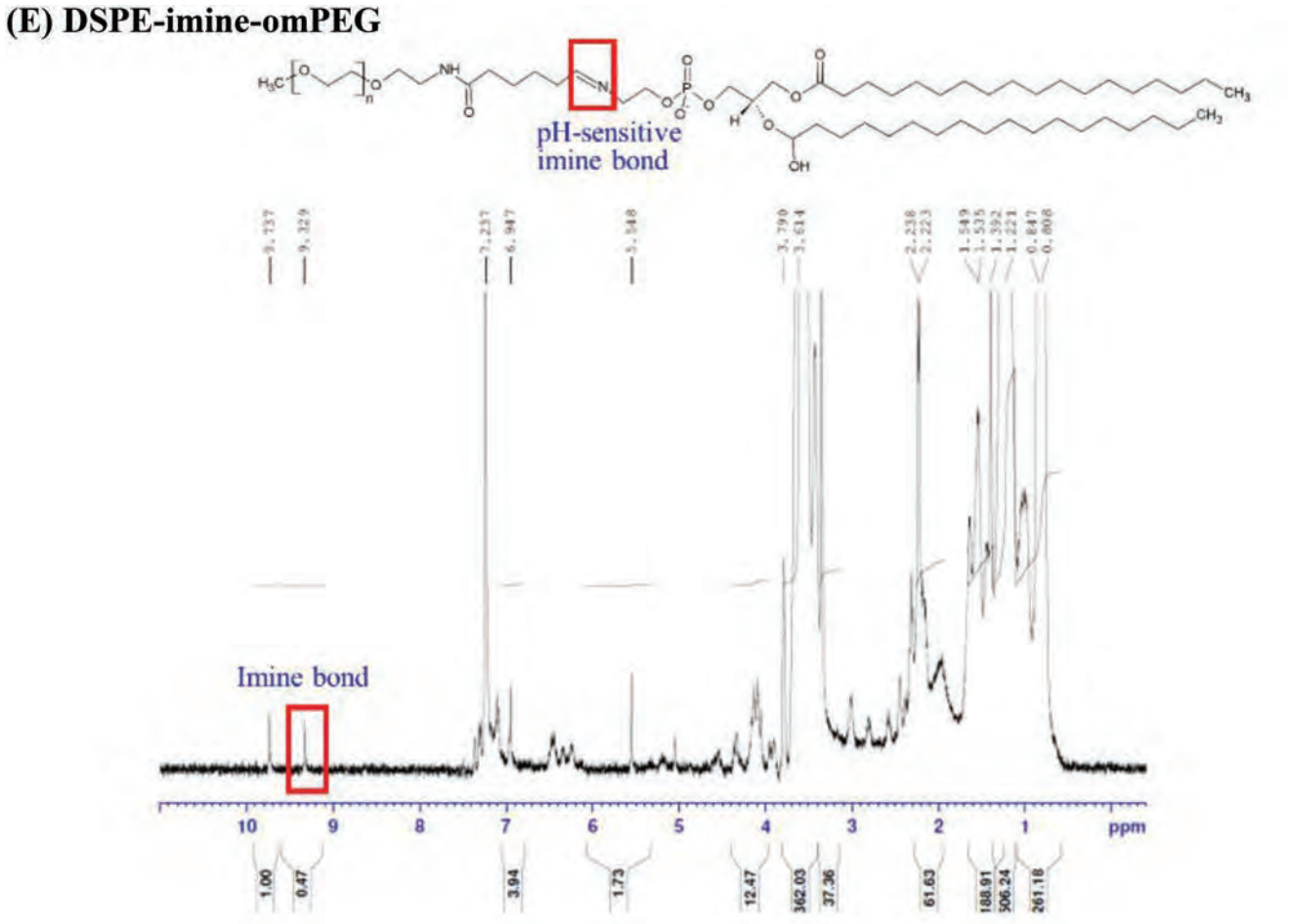

Figure 1. Continued.

targeted to mitochondria at 30 min (Figure 3D). DNR was then transported into the nucleus after 3 h-delivery and maintained in the nucleus up to 24 h after incubation of HCT116 cells with DNR/Lip-RFKH (Figure 3D).

2.4. Endocytosis Mechanisms for Uptake of Peptide-Modified Lip and SLN

According to the results shown in Figure S2D (Supporting Information), chlorpromazine (CPZ) and poly-L-lysine exhibited significant decreases in the relative fluorescence intensity % of DiI/Lip-RFKH in HCT116 cells after 3 h-incubation, suggesting that the cellular uptake of DiI/Lip-RFKH was primarily driven by clathrin- and adsorptive-mediated endocytosis, as supported by Figure S2D in the Supporting Information.

Furthermore, the efficiency % of HCT116 cell transfected with FAM-miR-200 by SLN-RFKH at 24 h was significantly greater than of Lipofectamine 3000, T-Pro P-Fect, PolyJet (served as positive controls), and naked FAM-miR-200, as detected by flow cytometric analysis (Figure 3E). However, Viromer displayed a transfection efficiency % compatible with that of SLN-RFKH (Figure 3E; $P > 0.05$). Moreover, upon visualization of the intracellular distribution of FAM-miR200/SLN-RFKH in HCT116 cells at 24 h via CLSM, clear uptake of FAM-miR200 (green fluorescence) was observed in the cytoplasm of HCT116 cells (Figure 3F). In addition to miR, the cell nuclei were stained with DAPI (blue), and lysosomes were stained with LysoTracker (red). It was obvious that FAM-miRNA-200 did not colocalize with lysosomes after 24 h of incubation (Figure 3F). Endo/lysosomal escape was thus verified, indicating that miR-200 was well-protected by SLN-RFKH to prevent miR-200 from degradation in endo/lysosomes.

Table 1. Characterization of peptide-modified liposomes incorporating irinotecan and solid lipid nanoparticles (SLN) encapsulating miR-200 ($n = 3$; values are mean ± SD).

	Size [nm]	PDI	Zeta potential [mV]	Encapsulation efficiency %	Loading capacity %
Iri/omLip-RF+K+H	174.7 ± 1.13	0.11 ± 0.02	−8.27 ± 2.19	89.32 ± 1.84	14.28 ± 0.95
miR-200/ omSLN-RF+K+H	141.7 ± 3.75	0.12 ± 0.03	18.2 ± 1.25	89.73 ± 0.71	16.34 ± 1.28

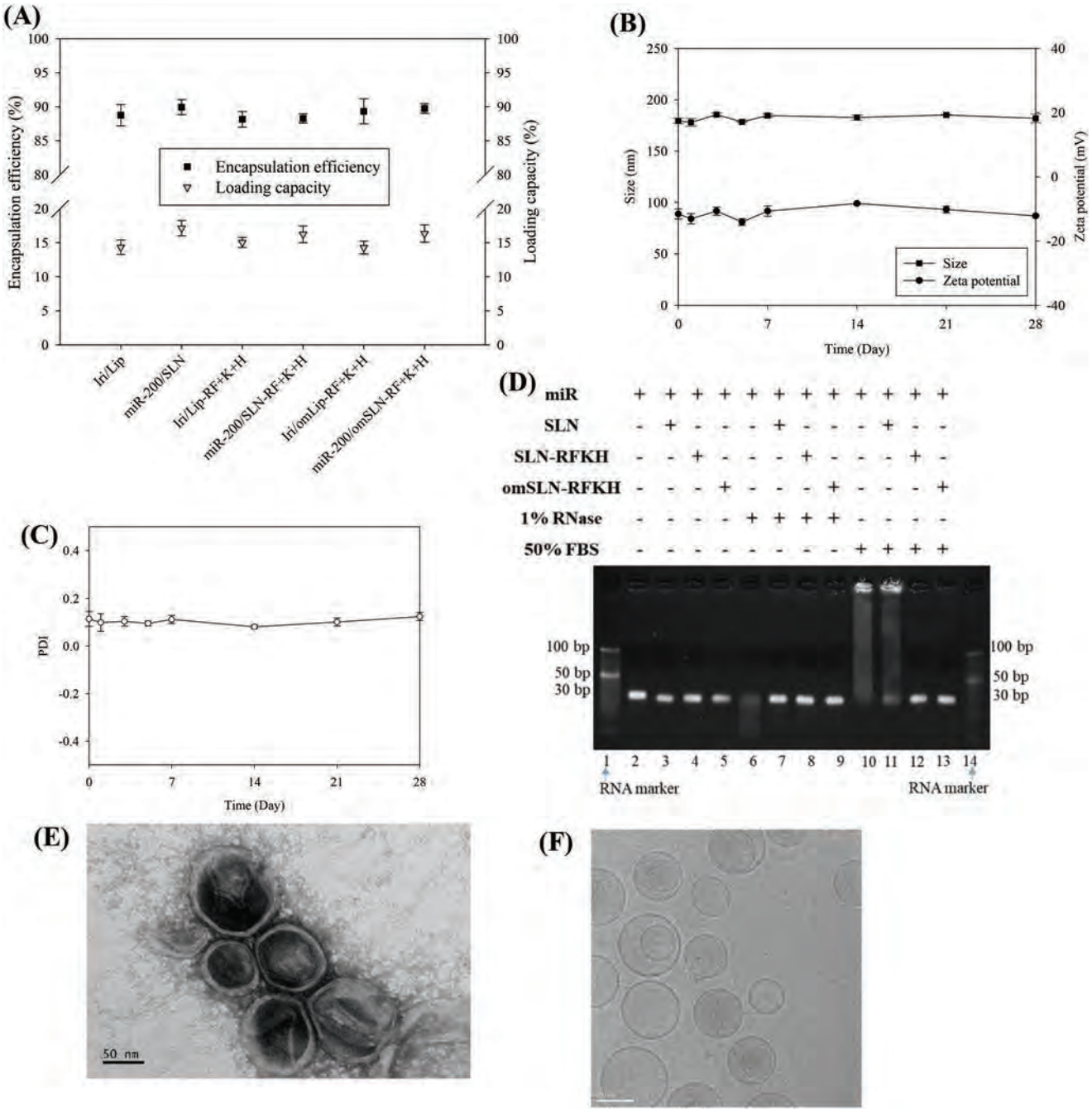

Figure 2. Characterization of various formulations. A) Encapsulation efficiency % and loading capacity %. B) Size, zeta potential, and C) PDI of Iri/omLip-RFKH at 4 °C for 28 d. Values are mean ± SD. D) Serum protection test of miR samples was monitored after incubation with 1% RNase or 50% FBS for 24 h. Lanes 2–5: no treatment; Lanes 6–9: 1% RNase treatment; Lanes 10–13: 50% FBS treatment; Lane 1 and 14: RNA marker. E) TEM images of Iri/omLip-RFKH. F) Cryo-TEM images of Iri/omLip-RFKH. Bar = 100 nm. For each group, $n = 3$.

2.5. Toxicity of Iri- or miR-Loaded Lip or SLN on Blood Cells, Intestinal Cells, and Cancer Cells

Nanoparticles were usually administered clinically by injection. Hence, hemolysis of Iri/Lip or miR/SLN was investigated using rat blood cells as a safety evaluation. As shown in **Figure 4**A, various Iri/Lip or miR/SLN formulations induced little hemolysis (3%–7%), revealing the acceptable safety of these tested liposomal and SLN formulations. Therefore, these modifications caused relatively low toxicity to blood cells. However, irinotecan showed ≈10% hemolysis, indicating slight toxicity (Figure 4A). Furthermore, irinotecan solution displayed ≈30% cytotoxicity to noncancerous IEC-6 cells, but irinotecan in Lip and Lip-RFKH reduced the cytotoxicity to about

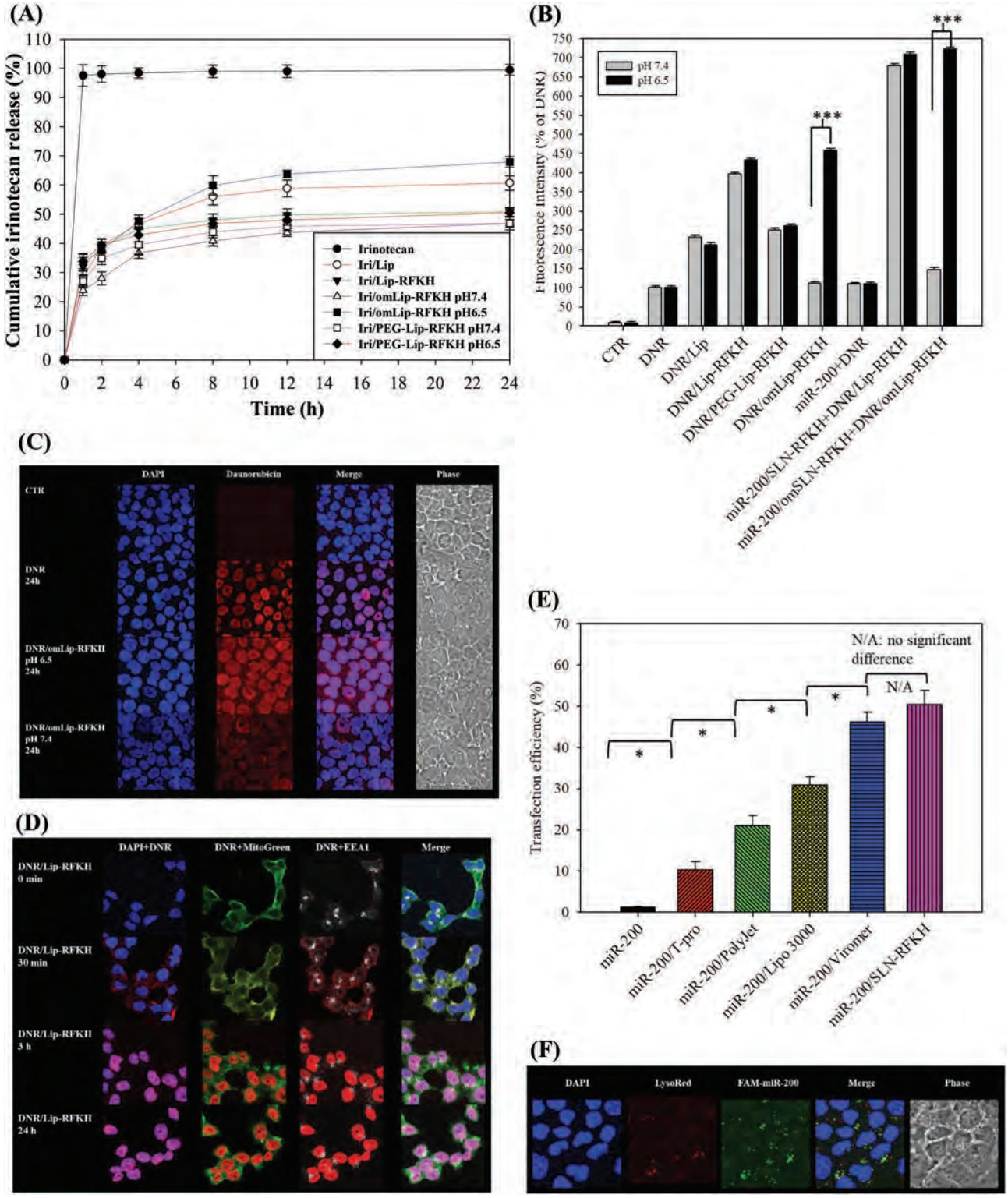

Figure 3. A–C) pH-sensitive profiles of various formulations. A) In vitro release of irinotecan with or without omLip-RFKH at pH 6.5 and 7.4. Iri/PEG-Lip-RKH was prepared by substituting DSPE-imine-PEG5000 into DSPE-PEG5000 (no pH-sensitive imine bond). B) Measurement of cellular uptake of daunorubicin (DNR; a probe of irinotecan) in various formulations into HCT116 cells at pH 6.5 and 7.4 by flow cytometry. C) The pH-responsive intracellular localization of DNR/omLip-RFKH in HCT116 cells by CLSM. D) The mitochondria-targeting and nuclear localization of DNR/Lip-RFKH in HCT116 cells by CLSM. DAPI: a nuclear dye; MitoGreen (MitoTracker Green): a mitochondrial dye; EEA1 (early endosome antigen 1): an early endosome marker. E) Transfection efficiency % of FAM-miR-200 by SLN-RFKH and commercial reagents in HCT116 cells by flow cytometry. $*P < 0.05$. F) CLSM images of FAM-miR-200/SLN-RFKH in HCT116 cells for 24 h. LysoRed (LysoTracker Red): a lysosomal dye.

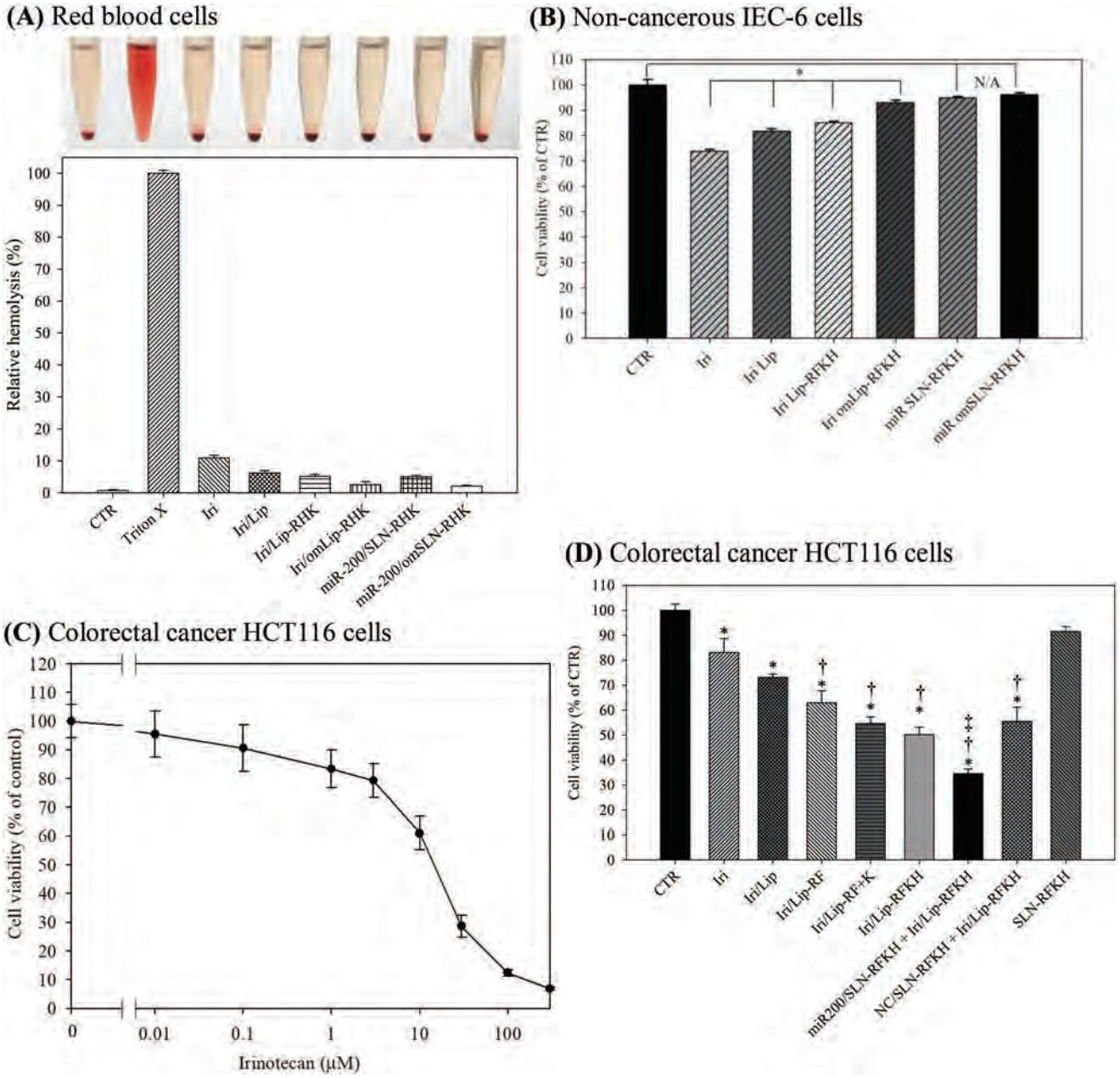

Figure 4. Cytotoxicity of various formulations on red blood cells, IEC-6, and HCT116 cells. A) Hemolysis effect of various formulations (upper panel). Hemoglobin release from rat blood cells was calculated (lower panel). For (B–D), the cell viability was determined by sulforhodamine B assay. Cytotoxicity of different formulations on B) IEC-6 cells and D) HCT116 cells for 48 h. $^{*}P < 0.05$ compared to CTR. $^{\dagger}P < 0.05$ compared to Iri/Lip. $^{\ddagger}P < 0.05$ compared to Iri/Lip-RFKH. NC: scrambled miRNA. C) The viability of HCT116 cells were treated with irinotecan in increasing concentrations for 48 h. D) miR-200/SLN-RFKH + Iri/Lip-RFKH: miR-200/SLN-RFKH first, followed by Iri/Lip-RFKH.

15%–20%. However, Iri/omLip-RFKH, miR-200 in SLN-RFKH, and omSLN-RFKH all displayed less than 10% toxicity to IEC-6 cells (Figure 4B), indicating the reduction in toxicity to intestinal epithelial cells.

Moreover, irinotecan showed a concentration-dependent inhibition on viability of HCT116 cells and irinotecan at 4×10^{-6} M exhibited ≈20% cytotoxicity in HCT116 cells (Figure 4C). Thus, this concentration was chosen to check the improvement by various liposomal formulations and/or combination with miR-200. As shown in Figure 4D, liposomes modified with RF+K and RF+K+H exhibited more cytotoxicity than liposomes modified with RF alone (both $P < 0.05$). The administration of miR-200/SLN-RFKH first and followed by Iri/Lip-RFKH exhibited the greatest inhibition percentage among all the groups (Figure 4D). Additionally, all the unmodified and peptide-modified Lip and SLN carriers showed marginal hemolysis effect to RBC cells and low cytotoxicity toward IEC-6 and HCT116 cells (Figure S3, Supporting Information).

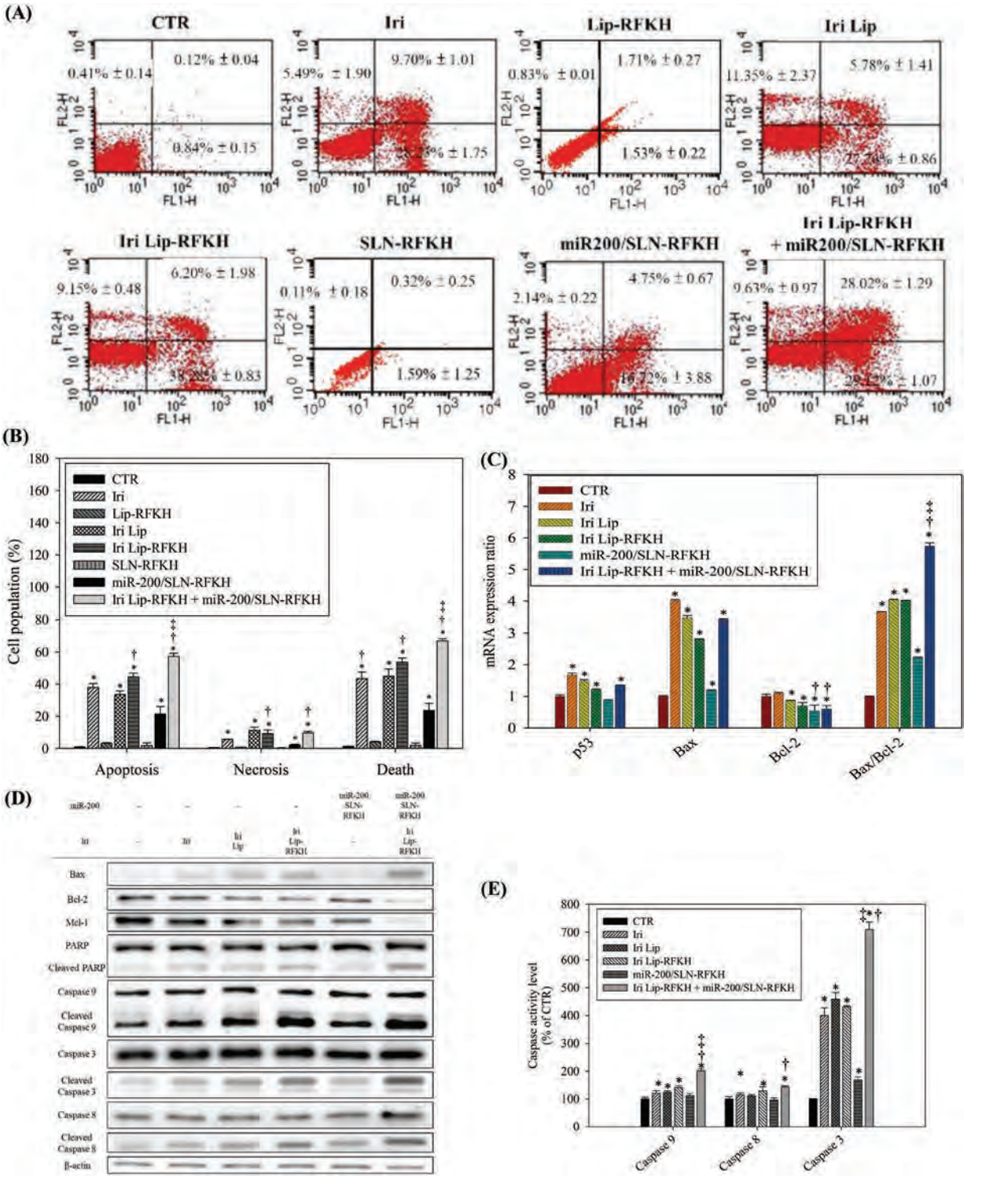

Figure 5. Effect of different formulations for 48 h on the death percentage, mRNA and protein expressions of apoptosis-associated pathway in HCT116 cells. A) Cell population distribution using annexin V/PI assay; B) The relative percentage of apoptosis, necrosis, and death of cell population; C) mRNA expression levels of p53, Bax, Bcl-2, and ratio of Bax/Bcl-2; D) The protein expression by western blotting. E) The activity levels of caspase-3, -8, -9.

2.6. Cell Death-Related Mechanisms

The apoptosis percentage (the sum of early and late apoptotic cells) and death percentage (the sum of apoptotic and necrotic cells; **Figure 5**A,B) induced by Iri/Lip-RFKH were both much higher than those induced by Iri/Lip. Furthermore, treatment of HCT116 cells with miR-200/SLN-RFKH followed by Iri/Lip-RFKH triggered the greatest induction (%) of apoptosis

and cell death in HCT116 cells (Figure 5A,B). Nevertheless, empty nanocarriers such as Lip-RFKH and SLN-RFKH exhibited negligible apoptosis, necrosis and death % (Figure 5A,B). Moreover, miR-200/SLN-RFKH+Iri/Lip-RFKH significantly intensified the Bax/Bcl-2 mRNA ratio (Figure 5C) and considerably upregulated the protein expression levels of Bax, cleaved PARP, and caspase-3, -8, and -9 (Figure 5D), as well as escalated the caspase-9 and caspase-3 activity levels to the greatest degree (Figure 5E). In contrast, Mcl-1 and Bcl-2 proteins were remarkably downregulated (Figure 5D).

2.7. Wnt/β-Catenin, MDR, and EMT-Associated Pathways

It has been reported that the Wnt/β-catenin and/or EMT pathways are potential targets of miR-200.[20] Iri/Lip-RFKH+miR-200/SLN-RFKH substantially inhibited the expressions of Rac1, KRAS, β-catenin, c-Myc, P-gp, MRP1, MRP2, ZEB1, Vimentin, and Slug compared with other treatment groups (**Figure 6**A–C). Excitingly, Iri/Lip-RFKH+miR-200/SLN-RFKH displayed significantly greater cell migration inhibition than other treatment groups (Figure 6D,E). Nonetheless, empty nanocarriers such as Lip, Lip-RFKH, and SLN-RFKH displayed insignificant inhibition in migration area % (Figure 6D,E).

2.8. In Vivo IVIS and PET/CT Imaging as well as Antitumor Efficacy and Biosafety Studies

Mice bearing colorectal CT26 tumor cells without treatment (CTR) displayed high fluorescence in the tumor region as shown by the IVIS images (**Figure 7**A). Furthermore, the images were normalized by IVIS software and the relative bioluminescence intensity is displayed in the lower panel of Figure 7A. Moreover, we used ^{18}F-FDG as a tool for detecting tumor proliferation change by PET/CT (Figure 7B) and 3D PET imaging (Figure S4, Supporting Information). The CT26 tumor-bearing mice treated with different Iri/Lip-RFKH and/or miR-200/SLN-RFKH formulations exhibited decreases in fluorescence and ^{18}F-FDG signals to various degrees around the tumor (Figure 7A,B; Figure S4, Supporting Information), while the mice treated with omLip-RFKH/Iri + omSLN-RFKH/miR-200 showed the most significant reduction in tumor fluorescence and ^{18}F-FDG retention (Figure 7A,B; Figure S4, Supporting Information). Moreover, the tumor size treated with pH-sensitive omLip-RFKH/Iri + omSLN-RFKH/miR-200 was 49.12% ± 5.83% of the original tumor volume on day 28, which was superior to all other treatments (Figure 7C).

For safety assessment, CT26-bearing mice treated with Iri showed a continuous decrease in the body weight (Figure 7D). All other groups displayed constant increases in body weight with minor individual differences (Figure 7D). Furthermore, serum GPT, CRE, and CKMB levels were examined to evaluate liver, renal, and heart functions, respectively (**Figure 8**A–C). The results showed that serum GPT, CRE, and CKMB levels were provoked after treatment with Iri or Iri/Lip (Figure 8A–C), indicating substantial damage induced by Iri or Iri/Lip to the liver, kidney, and heart. However, the serum levels of GPT, CRE, and CKMB were significantly diminished after treatment with Lip-RFKH/Iri alone or in combination with SLN-RFKH/miR-200 (Figure 8A–C). Additional coating with the pH-sensitive PEG derivative induced the most remarkable decreases in the serum levels of the three biomarkers (Figure 8A–C).

Moreover, mouse tumors in the control group displayed a higher cell number and larger nuclei than those in other groups, as investigated using H&E staining of tumors (Figure 8D, the first panel). Among various treatment groups, the tumor tissues in the omLip-RFKH/Iri + omSLN-RFKH/miR-200 group exhibited the most remarkable nuclear sign of chromatin condensation (pyknosis; red circle), indicating tumor cell apoptosis and necrosis (Figure 8D, the first panel). Additional evidence of tumor apoptosis was verified for different treatment groups, especially in the final combination group, as exhibited in Figure S5 in the Supporting Information. In contrast, H&E staining of intestines, kidney and liver of control groups showed good cell morphology (Figure 8D, 2–4 panels). The intestinal, renal, and liver tissues in the Iri, Iri/Lip, Iri/Lip-RFKH, and Iri/Lip-RFKH+miR-200/SLN-RFKH groups displayed interstitial hemorrhage (arrow), indicating tissue inflammation. The intestinal tissues also exhibited vacuoles (possible indication of fatty degeneration; blue circle), as well as a disordered cell arrangement, further suggesting intestinal injury and inflammation (Figure 8D, the second panel). Nevertheless, the group treated with omLip-RFKH/Iri + omSLN-RFKH/miR-200 demonstrated a remarkable reduction in interstitial hemorrhage and tissue degeneration, confirming a lessening of tissue injury and inflammation (Figure 8D, 2–4 panels).

3. Discussion

Irinotecan may penetrate and injure normal tissues, including mucosal membranes and results in unwanted side effects, such as diarrhea and vomiting.[6] MicroRNA also shows the disadvantages of rapid degradation and poor cellular uptake.[11] Hence, it is necessary to develop a pH-sensitive and tumor-targeting delivery system with good penetration for irinotecan and miR to improve the treatment of advanced CRC, as indicated in Figure 1A.

In the present study, Lip and SLN were successfully modified with cell-penetrating RF peptide, NG2-targeting H peptide, and mitochondria-targeting K peptide (Figure 1B–D). Furthermore, these nanoparticles were well-coated and shielded by outer pH-sensitive PEG layer (Figures 1E and 2D–F). Especially, miR was protected by pH-sensitive PEG and/or peptide modification in omSLN-RFKH from degradation or aggregation by the attack of RNase or extreme high concentration of FBS (Figure 2D), indicating that these pH-responsive and peptide-conjugated nanoparticles may provide an excellent platform for the parenteral administration of gene therapeutics such as miR. RF peptide possesses better cell selectivity than TAT peptide, a well-known CPP, by showing lower uptake into normal cells and higher uptake into tumor cells.[16,21] In our previous study, gefitinib encapsulation in PEGylated liposomes with surface modification by RF enhanced gefitinib transport across the blood–brain barrier (BBB) by modulating the transcytosis pathway(s) and thus further increased gefitinib cytotoxicity against lung cancer cells.[22] Additionally, K peptide triggered the mitochondrial-induced apoptotic pathway and inhibited tumor growth.[23]

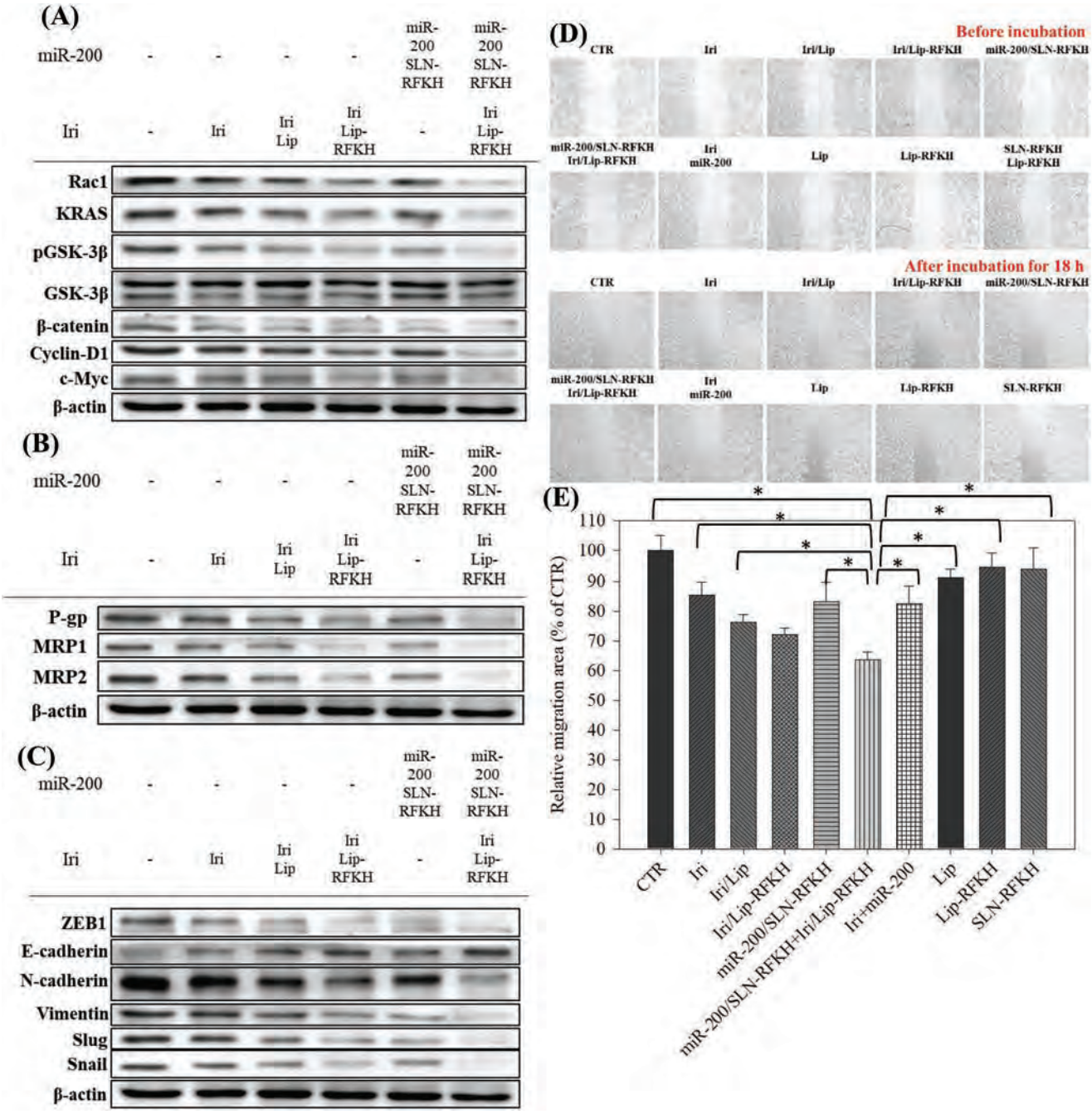

Figure 6. Effects of various formulations on the protein expressions of different pathways, and relative migration percentage. Expressions of A) Wnt/β-catenin pathway, B) MDR pathway, and C) EMT pathway by western blotting. D) Migration assay after various treatments for 18 h. E) Relative migration %.

K peptide also demonstrates the advantages of chemical stability, high antiproliferation activity, and specific disruption of mitochondrial membranes in cancer cells.[24] Moreover, the addition of H peptide can enhance targeting to NG2 overexpressed on tumor vasculature but not on normal vasculature.[25] In the current study, we found that further modification of Iri/Lip-RF with peptide K and H to form Iri/Lip-RF+K+H additionally reduced the viability % of HCT116 cells compared with Iri/Lip-RF (Figure 4D).

The pH sensitivity of omLip-RFKH and omSLN-RFKH was confirmed by findings of the cumulative release (Figure 3A; Figure S2C, Supporting Information), cellular uptake (Figure 3B), and intracellular localization (Figure 3C,E). However, there was no pH-dependent release or cellular uptake of Iri, DNR, or miR from PEG-Lip-RFKH or PEG-SLN-RFKH (no imine bond; Figure 3A,B; Figure S2C, Supporting Information). We thus suggest that omLip-RFKH might function as a tumor-selective delivery system that decreases entry of

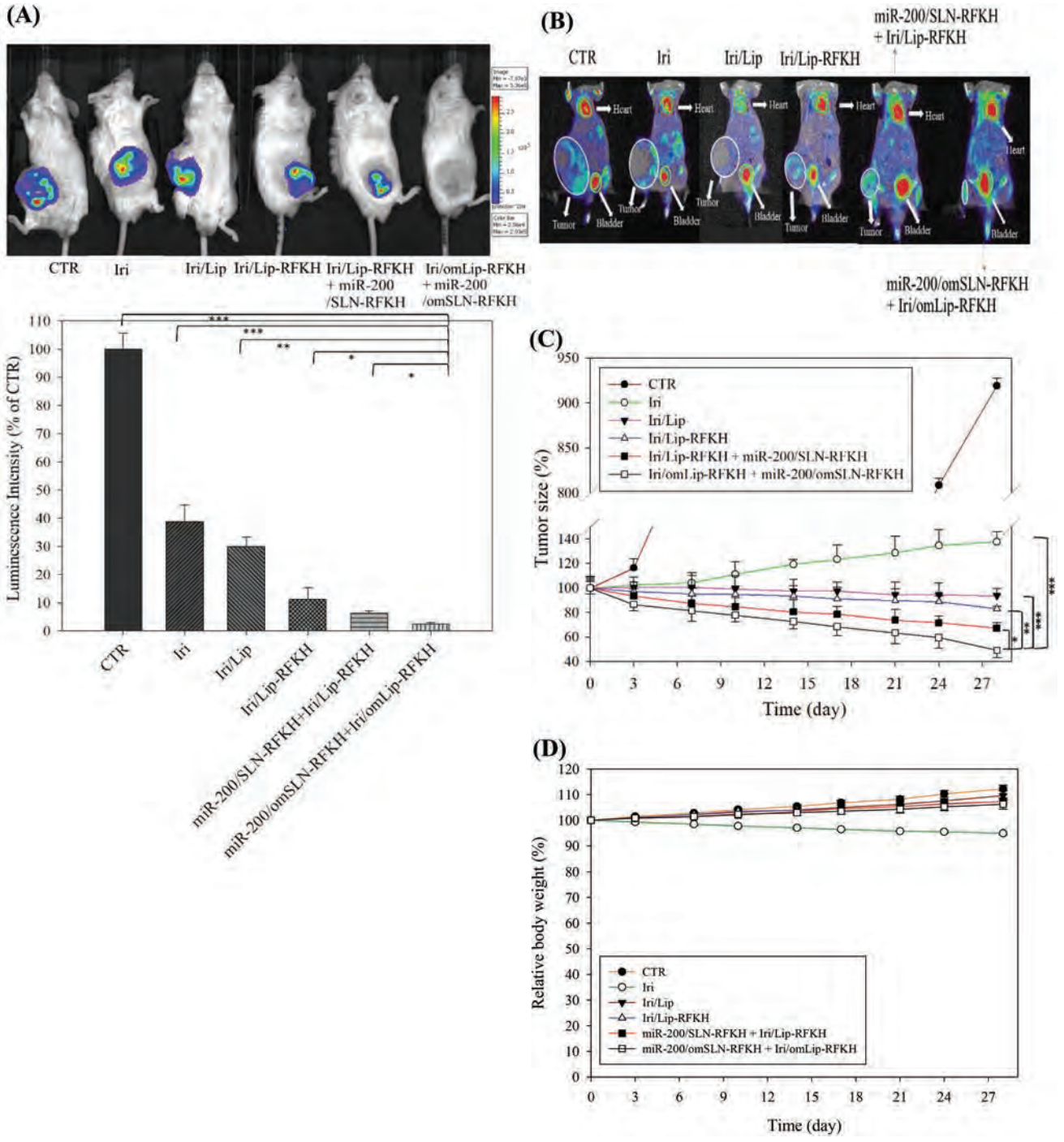

Figure 7. A) CT26-bearing mice were administered with various formulations once a week for 28 d. IVIS images of the mice in different groups were taken at the treatment end of 28 d. $n = 5$; the relative bioluminescence intensity is displayed in the lower panel. B) PET/CT images of the representative mice from each group. White circles: tumor; yellow circles: bladder; orange circles: heart C) Tumor size and D) body weight as a function of time in CT-26 bearing mice. $^{*}P < 0.05$; $^{**}P < 0.01$; $^{***}P < 0.001$.

therapeutics into normal tissues (pH 7.4) and increases their uptake at acidic tumor sites (pH 6.5). A similar finding using other pH-sensitive carriers has been reported in a previous study.[26] Moreover, when we observed the CLSM images, most DNR (a probe for irinotecan) released from omLip-RFKH at pH 6.5 appeared in the nucleus at 24 h (Figure 3C), revealing that these peptide-modified nanoparticles tended to successfully avoid drug entrapment by lysosomes and confirming an endosomal escape effect in agreement with a former study.[27] The mitochondria-targeting and nuclear localization of

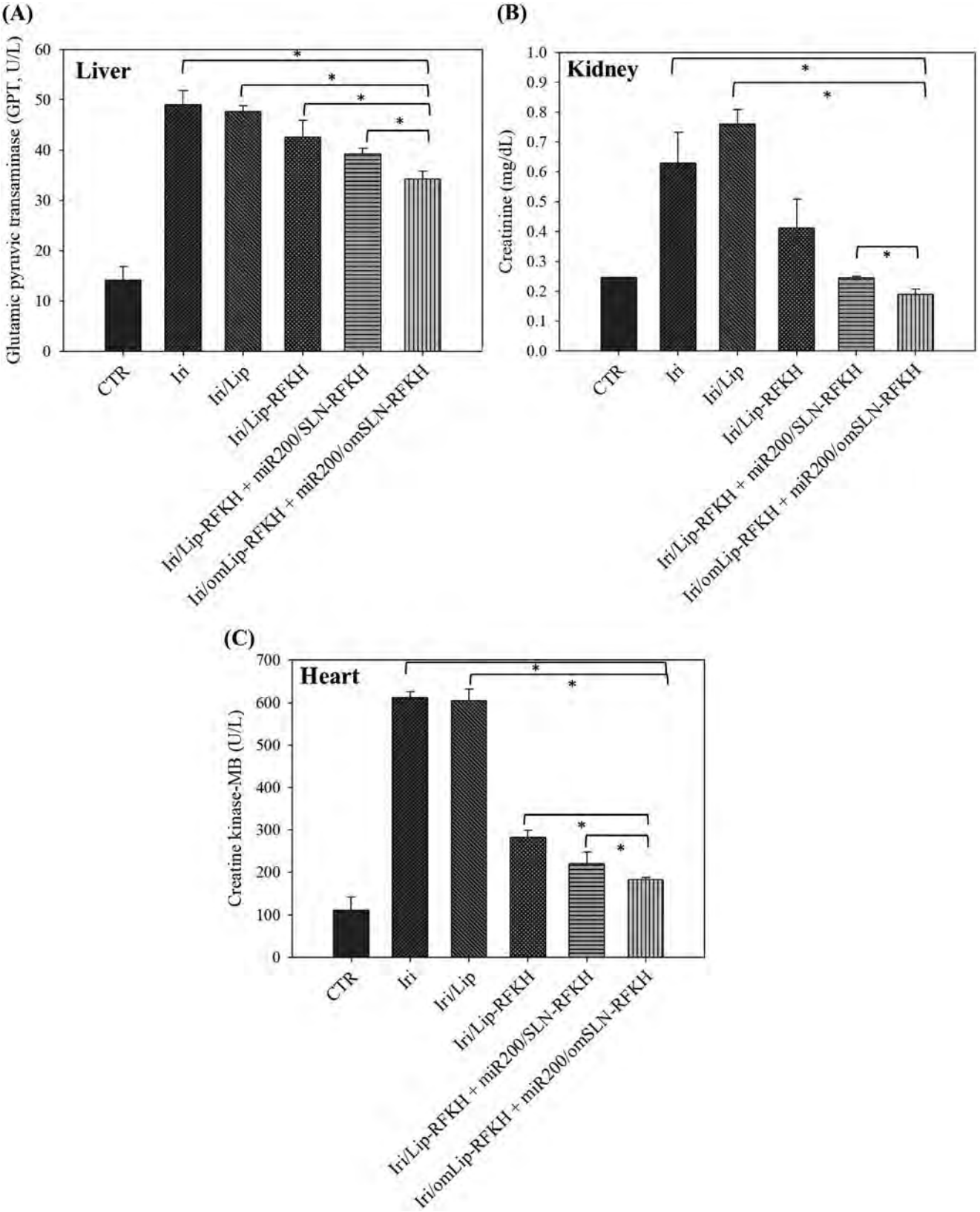

Figure 8. A) Serum levels of GPT, B) CRE, and C) CKMB at 48 h after last treatment of different formulations. D) Photomicrographs of H&E staining of mouse tissues. E) Scheme for modulation of multiple signaling pathways by Iri/Lip-RFKH+miR-200/SLN-RFKH in colorectal cancer model. NG2: nerve/glial antigen 2.

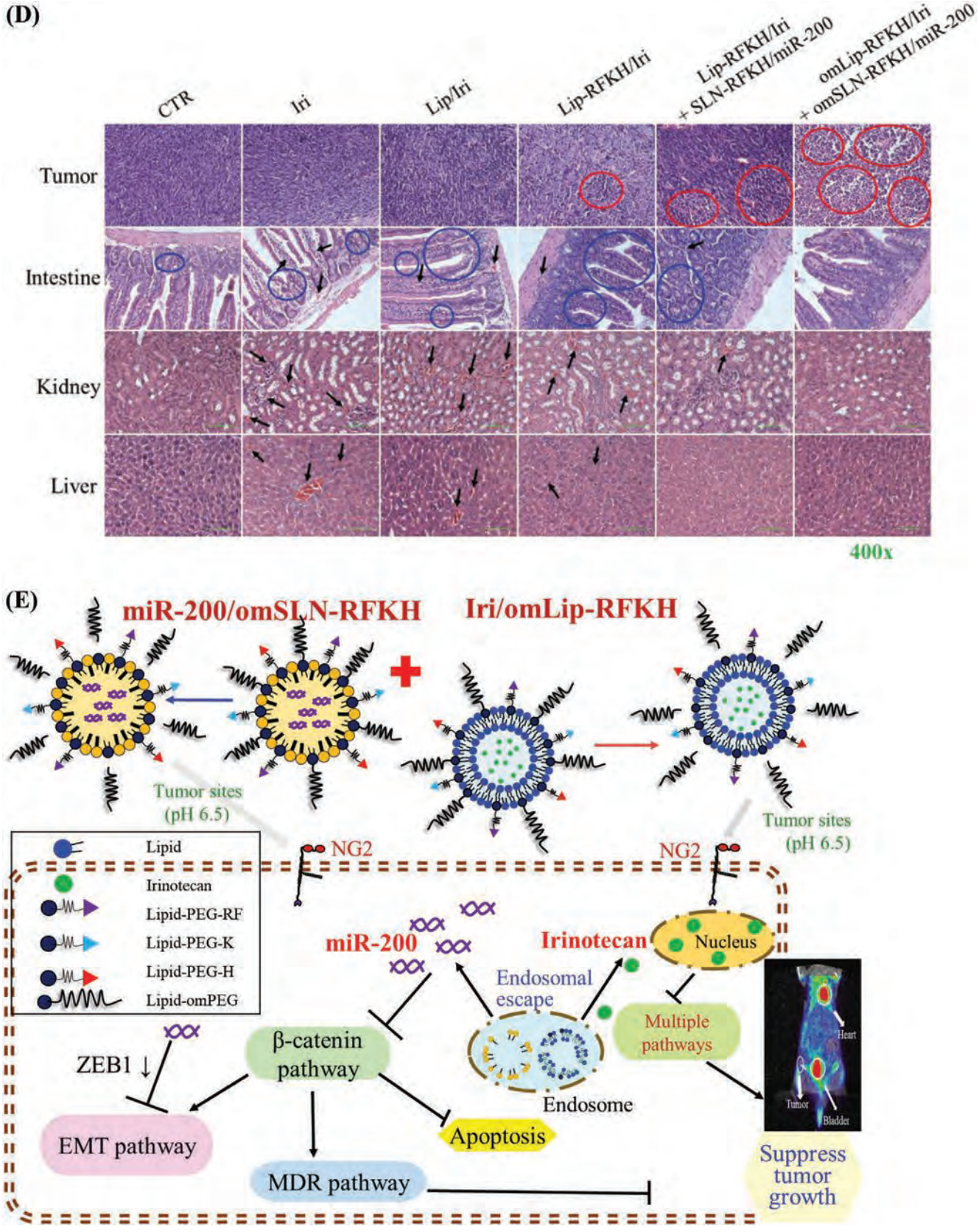

Figure 8. Continued.

DNR/Lip-RFKH in HCT116 cells were further verified using CLSM after 30 min, 3 h, and 24 h-incubation, as shown in Figure 3C,D. Consistently, we found that Lip-RFKH was preferentially taken up by HCT 116 cells through clathrin-dependent and adsorptive-mediated endocytosis pathways (Figure S2D, Supporting Information), which are reported to be the major endocytosis pathways for liposomes.[28] We suggest that the positively charged RF, H and K peptides on the liposome surface might increase the internalization of nanoparticles through adsorptive-mediated pathway.

The formulation of miR-200/SLN-RFKH improved the poor cellular uptake and enhanced the endosomal escape of miR-200, as validated in Figure 3E,F. Excitingly, the transfection efficiency % of SLN was greater or equal to that of commercial available Lipofectamine, PolyJet and Viromer (Figure 3E). The electrostatic interaction between the negative charges of miR-200 and the positive charges in SLN-RFKH allowed the formation of a stable complex. Another advantage of cationic nanoparticles is efficient endosomal escape via the proton sponge effect, leading to destabilization of endosomal membranes and improvement of gene transfer efficiency.[29] FAM-miR-200 (green) observed via CLSM was not colocalized with LysoTracker (red), indicating a good endosomal escape effect of miR-200 from SLN-RFKH to prevent miR damage in lysosomes (Figure 3F).

Apoptosis induced through PARP cleavage by irinotecan or its metabolite SN-38 has been demonstrated in colon carcinoma cells.[30] In the present study, combined treatment with miR-200/SLN-RFKH intensified the cytotoxicity of Iri/Lip-RFKH against HCT116 cells (Figure 4D). Irinotecan-induced tumor cell death primarily occurred via apoptosis induction and partially via necrosis, as supported by our results shown in Figure 5. Furthermore, the increase in the % of cells undergoing apoptosis and cell death was the most significant in the Iri/Lip-RFKH+miR-200/SLN-RFKH group (Figure 5A,B). Previous investigations have indicated that Bax and caspase-9 are involved in triggering apoptosis caused by irinotecan.[30,31] Consistently, our results showed that the mRNA, protein expression and/or activity levels of Bax, cleaved PARP, and caspase-3 and -9 were highest in the Iri/Lip-RFKH+miR-200/SLN-RFKH group among different treatments (Figure 5C–E).

Nevertheless, one of the major impediments to a successful response to irinotecan in human cancer patients is possibly due to the emergence of drug resistance.[4,32] Correspondingly, irinotecan, a P-gp and/or MRP substrate, is remarkably effluxed by upregulated pump proteins in CRC cells, and thus aggravates MDR in later stages of therapy.[5,6,33] Consequently, the therapeutic efficacy of irinotecan is decreased in MDR transporter-overexpressing cancer cells.[5] Reversal of resistance in CRC cells may require a new strategy of combined treatment. Interestingly, reprogramming HCT116 cells using miR-200 increased the sensitivity of cancer cells to 5-FU, possibly through suppression of MRP and c-Myc expression.[34] Moreover, transfection of breast cancer cells with miR-200 was found to enhance the chemosensitivity of cancer cells to epirubicin and reduce expression of P-gp.[35] Our present study further supported that miR-200 regulates the mRNA and protein expression of P-gp and MRPs, especially by Iri/Lip-RFKH+miR-200/SLN-RFKH treatment (Figure 6B).

The WNT/β-catenin signaling pathway plays a critical role in cell proliferation, differentiation, adhesion, and migration.[20] miR-200 family members have been shown to impede EMT and cancer cell migration by targeting the EMT transcription factors ZEB1/2 or by direct binding and blocking β-catenin translation.[20,36] Moreover, our previous findings demonstrated that inhibition of ABC transporters and modulation of the β-catenin/GSK-3β pathway sensitizes MDR human colon cancer Caco-2 cells to epirubicin.[37] In agreement with this previous evidence, the current study indicated that the protein expression of Rac1, KRAS and p-GSK 3β, β-catenin, cyclin D1, and c-Myc was diminished in HCT116 cells treated with Iri/Lip-RFKH+miR-200/SLN-RFKH (Figure 6A). Furthermore, miR-200/SLN-RFKH assisted in potentiating the migration inhibition triggered by Iri/Lip-RFKH (Figure 6D,E). In addition, E-cadherin upregulation through ZEB1 downregulation was also reported to restore cancer cell sensitivity to chemotherapy.[36,38] Accordingly, the decreases in migration% and the inhibition of EMT proteins such as ZEB 1 and vimentin by miR-200/SLN-RFKH and/or Iri/Lip-RFKH to various degrees were verified in our study (Figure 6C–E).

Another problem solved in the current study was the toxicity associated with cationic gene delivery systems or chemotherapeutic agents, such as irinotecan (Figures 4A,B, 7D, 8A–D; Figure S3, Supporting Information). Although our miR-200/SLN-RFKH exhibited a positive charge and Iri/Lip-RFKH demonstrated a negative charge (Table 1), these formulations showed low toxicity to both intestinal and blood cells (Figure 4A,B; Figure S3A,B, Supporting Information). All the hemolysis percentage values of the prepared Lip and SLN formulations were lower than 10% (Figure 4A; Figure S3A, Supporting Information), which follows the guideline suggesting that formulations must display hemolysis values of <10% to be considered nonhemolytic, while formulations with values >25% may have a risk of hemolysis.[39,40] Furthermore, lower toxicity of Iri/omLip to IEC-6 cells compared with Iri, indicating that omLip might reduce irinotecan's GI side effects (Figure 4B). Our in vivo results also suggested that omLip-RFKH and omSLN-RFKH were well tolerated and biocompatible (Figure 8D). The shielding by pH-sensitive omPEG-lipid layer to release less cargos to normal cells might reduce the toxicity. The remarkable declines in vacuoles, interstitial hemorrhage, tissue degeneration, and serum levels of GPT, CRE, and CKMB suggest the mitigation of tissue injury and inflammation after the pH-responsive PEG coating (Figure 8A–D). Hence, the application of Iri/omLip-RFKH alone or in combination with miR-200/omSLN-RFKH may benefit from the diminished adverse events such as GI toxicity and thus may increase their clinical implications. However, the tumor cells exhibited the morphological features of pyknosis, demonstrating tumor necrosis and apoptosis after various treatments, especially in the group of Iri/Lip-RFKH+miR-200/SLN-RFKH (Figure 8D, first panel). Tumor apoptosis was particularly noticeable for this combined treatment group, as exhibited in Figure S5 in the Supporting Information).

Furthermore, the most profound reduction in tumor signal was observed in the miR-200/omSLN-RFKH + Iri/omLip-RFKH treatment group via IVIS and PET/CT images (Figure 7A,B; Figure S4, Supporting Information). Moreover,

the anticancer efficacy and evidence of tumor cell apoptosis and necrosis were also verified by tumor size measurement (Figure 7C) and tumor HE staining (Figure 8D, first panel) and TUNEL assay (Figure S5, Supporting Information). The overall scheme for modulation of multiple signaling pathways by the combination of a cleavable PEG coating on peptide RFHK-modified Lip and SLN incorporating irinotecan and miR-200 in a colorectal cancer model is shown in Figure 8E.

4. Conclusion

Collectively, after combined treatment with Iri/Lip-RFKH+miR-200/SLN-RFKH, CRC cell growth was significantly reduced and the anticancer efficacy was remarkably enhanced in colon tumor-bearing mice. Apoptosis was the major mechanism involved in colon cancer cell death. Overall, successful delivery of miR-200 by omSLN-RFKH and irinotecan by omLip-RFKH modulated the β-catenin/MDR/apoptosis/EMT signaling pathways and suppressed the expression of Rac-1, KRAS, p-GSK-3β, β-catenin, cyclin D1, c-Myc, P-gp, MRPs, ZEB1, Slug, and Vimentin, thus effectively inhibiting tumor growth in colorectal cancer.

5. Experimental Section

More detailed description of material and method is reported in the Supporting Information.

Preparation of Irinotecan-Loaded Lip: Lip were prepared via the thin film hydration method. Briefly, DSPC, cholesterol, DSPE-PEG-peptide, and DSPE-omPEG (at a molar ratio of 1: 0.1: 0.1: 0.1: 0.1; synthesized as described in the Supporting Information) were dissolved in methanol/dichloromethane (1:9). After removal of organic solvent, the lipid film was resuspended in PBS. The mixture was extruded through 400, 200, and 100 nm membrane filter.

For preparation of drug-loaded Lip, irinotecan was added to the blank liposomes using an ammonium sulfate gradient method to obtain irinotecan-loaded liposomes.

Preparation of miR-Incorporated SLN: Solid lipid nanoparticles were prepared by aqueous solvent diffusion. L-α-Phosphatidylcholine (PC), cholesterol, DOTAP, DSPE-PEG-peptide, and DSPE-omPEG at a molar ratio of 1: 0.1: 0.1: 0.1: 0.1, respectively, were dissolved in methanol/dichloromethane (1:9). The resulting mixture was then dispersed rapidly into Tween 80 solution with stirring. Then, miRNA solution was added to the SLN colloidal dispersion, and the mixture was incubated at room temperature for 30 min.

Characterization of Lip and SLN: The size distribution and zeta potential were measured using a Zetasizer (Malvern). The morphology of Lip and SLN was observed under a TEM (JEOL). Additionally, the morphology was detected using a cryo-TEM instrument (FEI).

Encapsulation Efficiency (EE %) and Drug Loading Capacity (DL%): After centrifuge, irinotecan or miR in both the filtrate and nanoparticles was analyzed via HPLC (Hitachi). The flow rate was 1.0 mL min^{-1} and the detection wavelength was 220 nm. EE% and DL% were calculated using the equation shown below

$$\mathrm{EE\%} = \left[\left(W_e - W_f\right)/W_e\right] \times 100\% \quad (1)$$

$$\mathrm{DL\%} = \left[\left(W_e - W_f\right)/W_t\right] \times 100\% \quad (2)$$

where W_e is the weight of added irinotecan or miR, W_f is the weight of irinotecan or miR in the filtrate, and W_t is the total nanoparticle weight.

MicroRNA Protection Assay: Different formulations of miR in SLN were incubated with 1% RNase or 50% FBS at 37 °C for 24 h. After incubation, gel retardation assay was performed to analyze all the samples. The samples were run by 5% agarose gel at 120 V for 30 min. The gel was visualized and scanned by a gel documentation system (DigiGel; TopBio, Taipei, Taiwan).

pH-Sensitive Release: Irinotecan- or miR-loaded formulations were placed in a dialysis bag (1000-3500 MWCO) and dialyzed separately against PBS at pH 7.4 and 6.5. At the indicated time, solution was withdrawn from the incubation medium. The irinotecan concentrations were determined by HPLC to calculate the cumulative drug release %.

Cell Lines: HCT116 and CT26, human colorectal cancer and mouse colon adenocarcinoma cell lines, respectively, were obtained from the Food Industry Research and Development Institute (Hsinchu City, Taiwan). The cells were cultured in Dulbecco's modified Eagle's medium (DMEM) supplemented with 10% fetal bovine serum in an incubator with 5% CO_2 at 37 °C.

pH-Responsive Cellular Uptake and Intracellular Localization: Daunorubicin (DNR) was used as a fluorescent probe for irinotecan. Accumulation of DNR from different Lip in HCT116 cells was measured and observed using a FACSCalibur flow cytometer (Becton Dickinson) and an Olympus CLSM, respectively. After incubation with different treatments at pH 7.4 and 6.5 for 24 h, the cells were stained with DAPI (Sigma), a nuclear dye. Fluorescence observation was carried out using CLSM. For verification of characteristics of mitochondria-targeting and endosomal escape, a mitochondrial dye, MitoTracker Green (ThermoFisher) and an antibody for early endosome antigen 1 (EEA1; Cell signaling) were used.

Cell Viability: The cytotoxicity of formulations in rat small intestinal epithelial IEC-6 cells and human colorectal cancer HCT116 cells was determined using a sulforhodamine B (SRB) assay. After 48 h incubation with various formulations, the cells were stained with SRB for 10 min. The absorbance at 540 nm was detected with a microplate TECAN reader.

Western Blotting: After treatment with different formulations for 48 h, the protein samples were separated via SDS-PAGE and transferred onto a polyvinylidene difluoride membrane (Bio-Rad) at 80 V. After blocking, blots were incubated with primary antibodies from Cell Signaling or Abcam and horseradish peroxidase-conjugated goat anti-rabbit IgG (Jackson) and developed using an detection system (Millipore). The membrane was reprobed with anti-β-actin antibody and monitored using an enhanced chemiluminescence detection kit (PerkinElmer).

Migration Assay: After different treatments, the cells in inserts were monitored for 18 h. The blank area was quantified using ImageJ and the migration area percentage was calculated.

$$\text{Migration area}\left(\%\text{ of area at 0 h}\right) = 100\% - \left(\text{Blank area}_{(18\,\text{h})}/\text{Blank area}_{(0\,\text{h})} \times 100\%\right) \quad (3)$$

Establishment of In Vivo Mouse Tumor Model: Male BALB/c mice at the age of 6 weeks with body weights of 20 ± 2 g were purchased from National Laboratory Animal Center (Taipei, Taiwan) and maintained in an individual ventilation cage system. The animals were ensured free access to sterilized food and water. CT-26 (10^5 cells in 0.1 mL PBS) were injected subcutaneously into the right flank of mice to obtain tumor-bearing BALB/c mice. All processes performed on the animals were in accordance with the National Institutes of Health Guide for the Care and Use of Laboratory Animals and were approved by the National Yang-Ming University Animal Committee.

IVIS Imaging: CT-26 cells (10^5 cells in 0.1 mL PBS) were injected subcutaneously into the right flank of mice to obtain tumor-bearing BALB/c mice. When tumor volume reached ≈100 mm^3 (Equation (4)), the mice were randomly assigned to six groups ($n = 5$ for each group). Group 1 was treated with saline solution (CTR), group 2: Iri solution, group 3: Iri/Lip, group 4: Lip-RFKH/Iri, group 5: miR-200/SLN-RFKH + Iri/Lip-RFKH (miR-200/SLN-RFKH first followed by Iri/Lip-RFKH), and group 6: miR-200/omSLN-RFKH + Iri/omLip-RFKH. Mice were injected intravenously (IV) with Iri at 100 mg per kg and miR-200 at 1.25 mg per kg in different formulations every 7 d for 28 d. Fluorescence images were visualized one day after the final treatment using an IVIS SPECTRUM (Caliper).

$$V = \left(L \times W^2\right)/2 \quad (4)$$

where length (*L*, mm) is the longest diameter and width (*W*, mm) is the shortest diameter perpendicular to the length axis.

Positron Emission Tomography/Computed Tomography (PET/CT): Tumor images were monitored using PET/CT. One day after the final treatment (at day 28), mice were injected intravenously with 0.282 mCi [^{18}F]-fluorodeoxyglucose (^{18}F-FDG). Images were acquired using a LabPET/X-SPECT/X-O CT imaging system (TriFoil Imaging, Inc., USA) at 30 min after injection of ^{18}F-FDG.[41] In addition, CT acquisitions were conducted for 3 min (FOV = 80 mm) after each PET scan to detect anatomical information for each animal and construct an attenuation map for further image restoration. PET and CT images were observed and computed using AMIDE software (SourceForge, Iowa, USA).

Assessment of In Vivo Antitumor Efficacy and Body Weight: Animal body weight and tumor size were detected every 3 or 4 d for 28 d. Tumor size was measured with a digital caliper and the tumor volume (*V*) was calculated (Equation (4)).

Biochemical Tests and Hematoxylin and Eosin (H&E) Staining: Tumor-bearing mice were treated as described above. Blood samples (170 µL) were taken from the orbital sinus of mice 48 h after the final treatment. After harvesting and centrifugation for 15 min, liver, kidney, and heart functions were assessed by detecting the serum levels of glutamate pyruvate transaminase (GPT), creatinine (CRE), and creatine kinase-MB (CK-MB) using corresponding activity assay kits (Fujifilm, Tokyo, Japan) and a clinical dry chemistry analyzer (Fuji Dri-Chem 7000 V, Fujifilm Corp.). Additionally, the tumors and intestines were fixed in 4% paraformaldehyde overnight, embedded in paraffin, and cut into 5-µm-thick sections for H&E staining, and the histology of these samples was examined using an Olympus microscope.

TUNEL Assay: TUNEL assay was performed to assess in vivo apoptosis in CT26 tumor-bearing mice at 48 h after last treatment of different formulations.[42] In brief, the samples were frozen and fixed in 4% paraformaldehyde for 20 min. After washing with PBS for 10 min, the samples were immersed on ice for 2 min. After mixing with reaction dispersion (50 µL) according to the manufacture's manual (In Situ Cell Death Detection Kit, Roche, Germany), the section samples were stained with Hoechst in the nuclei for comparison and monitored using CLSM.

Statistical Analysis: Results are expressed as the mean ± standard deviation (SD). Statistical significance was analyzed using Student's *t*-test to compare differences between two treatment groups. Statistical analysis was also conducted using one-way ANOVA and Dunnett's multiple comparison tests. Differences were considered to be statistically significant if the *P*-value was less than 0.05.

Supporting Information

Supporting Information is available from the Wiley Online Library or from the author.

Acknowledgements

This project was financially supported by grants from Ministry of Science and Technology of Taiwan (MOST 106-2320-B-010-005; MOST 107-2320-B-010-015-MY3), Veterans General Hospitals and University System of Taiwan (VGHUST106-G7-7-3; VGHUST108-G2-1-2), National Yang-Ming University and Cheng Hsin General Hospital (CY10726; CY10839), Center for Advanced Pharmaceutics and Drug Delivery Research, School of Medicine (Development and Construction Plan), National Yang-Ming University, Ministry of Education of Taiwan (Aiming for the Top University Plan). The authors thank the Taiwan Animal Consortium (MOST 107-2319-B-001-002)-Taiwan Mouse Clinic for technical support in animal imaging experiments. The authors also thank Dr. Yuan-Chih Chang at the Institute of Cellular and Organismic Biology, Academia Sinica, Taipei, Taiwan for assisting in the operation of the cryo-TEM instrument.

Conflict of Interest

The authors declare no conflict of interest.

Keywords

chemotherapy, cleavable PEG shedding, colorectal cancer, combination therapy, microRNA, pH-sensitive targeting nanoparticles

Received: June 25, 2019
Revised: August 21, 2019
Published online:

[1] T. Yoshinaga, T. Shigemitsu, H. Nishimata, M. Kitazono, E. Hori, A. Tomiyoshi, T. Takei, M. Yoshida, *Mol. Clin. Oncol.* **2015**, *3*, 1080.
[2] Y. Du, W. Zhang, R. He, M. Ismail, L. Ling, C. Yao, Z. Fu, X. Li, *Bioorg. Med. Chem.* **2017**, *25*, 3247.
[3] Y. Xu, M. A. Villalona-Calero, *Ann. Oncol.* **2002**, *13*, 1841.
[4] M. M. Gottesman, T. Fojo, S. E. Bates, *Nat. Rev. Cancer* **2002**, *2*, 48.
[5] L. M. Negi, M. Jaggi, V. Joshi, K. Ronodip, S. Talegaonkar, *Int. J. Biol. Macromol.* **2015**, *72*, 569.
[6] L. M. Negi, S. Talegaonkar, M. Jaggi, A. K. Verma, R. Verma, S. Dobhal, V. Kumar, *Colloids Surf., B* **2014**, *123*, 610.
[7] C. Shi, F. Huang, X. Gu, M. Zhang, J. Wen, X. Wang, L. You, X. Cui, C. Ji, X. Guo, *Oncotarget* **2016**, *7*, 40830.
[8] B. Humphries, C. Yang, *Oncotarget* **2015**, *6*, 6472.
[9] M. Korpal, Y. Kang, *RNA Biol.* **2008**, *5*, 115.
[10] T. Arumugam, V. Ramachandran, K. F. Fournier, H. Wang, L. Marquis, J. L. Abbruzzese, G. E. Gallick, C. D. Logsdon, D. J. McConkey, W. Choi, *Cancer Res.* **2009**, *69*, 5820.
[11] M. A. Suliman, Z. Zhang, H. Na, A. L. Ribeiro, Y. Zhang, B. Niang, A. S. Hamid, H. Zhang, L. Xu, Y. Zuo, *Int. J. Mol. Med.* **2016**, *38*, 776.
[12] F. Wang, Y. Wang, X. Zhang, W. Zhang, S. Guo, F. Jin, *J. Controlled Release* **2014**, *174*, 126.
[13] M. A. Burg, R. Pasqualini, W. Arap, E. Ruoslahti, W. B. Stallcup, *Cancer Res.* **1999**, *59*, 2869.
[14] C. Brand, C. Schliemann, J. Ring, T. Kessler, S. Baumer, L. Angenendt, V. Mantke, R. Ross, H. Hintelmann, T. Spieker, E. Wardelmann, R. M. Mesters, W. E. Berdel, C. Schwoppe, *Oncotarget* **2016**, *7*, 6774.
[15] A. V. Suhovskih, S. V. Aidagulova, V. I. Kashuba, E. V. Grigorieva, *Cell Tissue Res.* **2015**, *361*, 833.
[16] K. Usui, T. Kikuchi, M. Mie, E. Kobatake, H. Mihara, *Bioorg. Med. Chem.* **2013**, *21*, 2560.
[17] L. Jiang, L. Li, X. He, Q. Yi, B. He, J. Cao, W. Pan, Z. Gu, *Biomaterials* **2015**, *52*, 126.
[18] J. Y. Kim, J. H. Han, G. Park, Y. W. Seo, C. W. Yun, B. C. Lee, J. Bae, A. R. Moon, T. H. Kim, *Oncotarget* **2016**, *7*, 32449.
[19] B. Law, L. Quinti, Y. Choi, R. Weissleder, C. H. Tung, *Mol. Cancer Ther.* **2006**, *5*, 1944.
[20] N. M. Ghahhari, S. Babashah, *Eur. J. Cancer* **2015**, *51*, 1638.
[21] H. Park, H. Tsutsumi, H. Mihara, *Biomaterials* **2014**, *35*, 3480.
[22] K. H. Lin, S. T. Hong, H. T. Wang, Y. L. Lo, A. M. Lin, J. C. Yang, *Int. J. Mol. Sci.* **2016**, *17*, 1998.
[23] W. Qifan, N. Fen, X. Ying, F. Xinwei, D. Jun, Z. Ge, *Tumor Biol.* **2016**, *37*, 10643.
[24] K. E. Burns, T. P. McCleerey, D. Thevenin, *Sci. Rep.* **2016**, *6*, 28465.
[25] Y. Y. Guan, X. Luan, J. R. Xu, Y. R. Liu, Q. Lu, C. Wang, H. J. Liu, Y. G. Gao, H. Z. Chen, C. Fang, *Biomaterials* **2014**, *35*, 3060.
[26] Y. T. Chiang, C. L. Lo, *Biomaterials* **2014**, *35*, 5414.
[27] M. Yuan, Y. Qiu, L. Zhang, H. Gao, Q. He, *Drug Deliv.* **2016**, *23*, 1171.

[28] L. Brodin, P. Low, O. Shupliakov, *Curr. Opin. Neurobiol.* **2000**, *10*, 312.
[29] W. Chen, H. Li, Z. Liu, W. Yuan, *Front. Aging Neurosci.* **2016**, *8*, 68.
[30] Y. Takeba, S. Sekine, T. Kumai, N. Matsumoto, S. Nakaya, Y. Tsuzuki, Y. Yanagida, H. Nakano, T. Asakura, T. Ohtsubo, S. Kobayashi, *Biol. Pharm. Bull.* **2007**, *30*, 1400.
[31] R. Ravi, A. J. Jain, R. D. Schulick, V. Pham, T. S. Prouser, H. Allen, E. G. Mayer, H. Yu, D. M. Pardoll, A. Ashkenazi, A. Bedi, *Cancer Res.* **2004**, *64*, 9105.
[32] E. Filipski, E. Berland, N. Ozturk, C. Guettier, G. T. van der Horst, F. Levi, A. Okyar, *Toxicol. Appl. Pharmacol.* **2014**, *274*, 471.
[33] X. Y. Chu, H. Suzuki, K. Ueda, Y. Kato, S. Akiyama, Y. Sugiyama, *J. Pharmacol. Exp. Ther.* **1999**, *288*, 735.
[34] S. Miyazaki, H. Yamamoto, N. Miyoshi, X. Wu, H. Ogawa, M. Uemura, J. Nishimura, T. Hata, I. Takemasa, T. Mizushima, M. Konno, Y. Doki, M. Mori, H. Ishii, *Ann. Surg. Oncol.* **2015**, *22*, 1394.
[35] M. Lerner, M. Haneklaus, M. Harada, D. Grander, *PLoS One* **2012**, *7*, e36490.
[36] M. Mutlu, U. Raza, O. Saatci, E. Eyupoglu, E. Yurdusev, O. Sahin, *J. Mol. Med.* **2016**, *94*, 629.
[37] Y. K. Lee, T. H. Lin, C. F. Chang, Y. L. Lo, *PLoS One* **2013**, *8*, e82478.
[38] S. Tanaka, M. Hosokawa, T. Yonezawa, W. Hayashi, K. Ueda, S. Iwakawa, *Biol. Pharm. Bull.* **2015**, *38*, 435.
[39] K. Amin, R. M. Dannenfelser, *J. Pharm. Sci.* **2006**, *95*, 1173.
[40] M. A. Dobrovolskaia, J. D. Clogston, B. W. Neun, J. B. Hall, A. K. Patri, S. E. McNeil, *Nano Lett.* **2008**, *8*, 2180.
[41] T. C. Liu, Y. C. Lee, C. Y. Ko, R. S. Liu, C. C. Ke, Y. C. Lo, P. S. Hong, C. Y. Chu, C. W. Chang, P. W. Wu, Y. Y. Chen, S. Y. Chen, *Theranostics* **2018**, *8*, 4210.
[42] Y. Pei, L. Chen, Y. Huang, J. Wang, J. Feng, M. Xu, Y. Chen, Q. Song, G. Jiang, X. Gu, Q. Zhang, X. Gao, J. Chen, *Small* **2019**, *15*, 1900631.